

1 **The Dynamic Response of Floating Offshore Wind Turbine**
 2 **Platform in Wave-current Condition**

3
 4 Xiang Li (李翔)¹, Qing Xiao (肖清)^{1*}, Enhao Wang (王恩浩)², Christophe Peyrard³,
 5 Rodolfo T. Gonçalves⁴

6 ¹Department of Naval Architecture, Ocean and Marine Engineering, University of
 7 Strathclyde, Glasgow, UK

8 ²Tsinghua Shenzhen International Graduate School, Shenzhen, China

9 ³Saint-Venant Hydraulics Laboratory (Électricité de France, ENPC), Université Paris
 10 Chatou, France

11 ⁴OSPL - Ocean Space Planning Laboratory, Department of Systems Innovation, School
 12 of Engineering, The University of Tokyo, Tokyo, Japan

13

14 **Abstract**

15 In this paper, the fluid-structure interaction (FSI) of floating offshore wind turbine
 16 (FOWT) platforms under complex ocean conditions is investigated using OpenFOAM
 17 and in-house developed models. Two types of FOWT platform, i.e., a semi-submersible
 18 platform and a barge platform, are studied for their dynamic responses to either wave
 19 or current. Results reveal that a semi-submersible platform exhibits larger cross-flow
 20 (CF) motion and lock-in phenomenon, while a barge platform experiences smaller
 21 motion with no significant lock-in within the velocity range examined. The combined
 22 wave-current conditions are further studied for the semi-submersible platform, with
 23 different angles between wave and current, the current speeds and wave parameters.
 24 Unlike other investigations focusing on colinear wave-current interaction, in which the
 25 waves usually mitigate vortex-induced-motion (VIM), here, we find that waves might
 26 lead to an enhanced VIM with a large angle between current and wave. The evaluation
 27 on the interaction effect factor (IEF) shows that the largest wave height in the lock-in
 28 region doesn't lead to the most dangerous scenario, herein, the largest platform motion.
 29 Instead, a smaller wave height with large wave period can induce even larger motion.

30

31

32 The author with * is the corresponding author: Qing Xiao: qing.xiao@strath.ac.uk

This is the author's peer reviewed, accepted manuscript. However, the online version of record will be different from this version once it has been copyedited and typeset.

PLEASE CITE THIS ARTICLE AS DOI: 10.1063/5.0158917

Accepted to Phys. Fluids 10.1063/5.0158917

1

2

I. INTRODUCTION

3

4

5

6

7

8

9

10

11

12

13

14

15

16

17

18

19

20

21

22

23

24

25

26

27

28

29

30

31

32

33

34

35

36

37

38

39

40

41

42

The increasing demand for renewable energy has led to the growth of wind energy, with floating offshore wind turbines (FOWTs) being a promising solution for generating energy in deep water where traditional turbines are unable to operate. FOWTs also benefit from greater and more consistent wind resources in deeper water and eliminate the visual impact associated with near-shore turbines^{1,2}. Several FOWT designs, such as OC4 DeepCwind³, Hywind⁴, TetraSpar⁵, among others, have been developed extensively. For FOWTs, their applications are expected to expand to more diverse locations, which may present more complex sea states, resulting in more significant challenges in ensuring adequate stability, power output and reliability under diverse operating conditions, for the design of FOWT, and this has been investigated extensively both numerically and experimentally in our previous studies⁶⁻⁸ and other researchers⁹⁻¹⁴.

In addition to wave-platform-interaction, the appearance of water current in some areas of sea may lead to additional platform motion, known as Vortex-induced Motion (VIM). This phenomenon usually occurs when a cylindrical structure or a bluff body is moored or elastically mounted in the presence of current. The amplitude of the response can be particularly high when the frequency of vortex shedding becomes synchronized with the structure vibration frequency^{15,16}. Such synchronization is known as lock-in, and it occurs over a wide range of flow velocity.

The VIM of cylinders and monocolumn platforms has been extensively studied experimentally¹⁷⁻¹⁹. It was found that the platform follows a classic 8-shaped orbital trajectory for some cases. This low-frequency response, especially in cross-flow (CF) direction, may result in potential damage to FOWT's mooring system and cause fatigue problem²⁰. The in-line (IL) motion is relatively small compared to that in CF direction.

Compared to wave, current-platform-interaction gets less attention during the design process of FOWT platform. This is partially because the water current caused by wind has a characteristic speed of 0.05 to 0.5 m/s, which is less than the minimal threshold required for VIM to occur. The speed of tidal current is usually larger than surface current, whose maximum value can be as large as 4.5 m/s as observed in some channel areas²¹, with a water depth ranging from 40-110 m, but this velocity is much smaller in deep, open ocean. However, in certain locations, such as the Gulf Stream, the current velocity at the free surface can exceed 2 m/s, which is sufficiently large to induce VIM for a floating platform having cylinders, such as SPAR²²⁻²⁴. The semi-submersible (SS) platform, on the other hand, has a smaller aspect ratio (draft/characteristic length), which has been investigated by Gonçalves et al.^{25,26}. Their experimental findings confirmed that VIM occurs even at a relatively low current speed for two SS platforms with different geometric dimensions. Other research regarding VIM of different

This is the author's peer reviewed, accepted manuscript. However, the online version of record will be different from this version once it has been copyedited and typeset.

PLEASE CITE THIS ARTICLE AS DOI: 10.1063/5.0158917

Accepted to *Phys. Fluids* 10.1063/5.0158917

1 platforms can also be found recently^{27,28}. Due to the inherent disadvantage of potential-
 2 flow theory method, in which fluid is assumed irrotational and non-viscous, numerical
 3 analysis involving offshore structure-fluid interaction has been conducted using finite
 4 element method²⁹ (FEM) or computational fluid dynamics (CFD) method. The later
 5 considers viscosity of fluid directly by solving Navier-stokes equation with turbulence
 6 models³⁰⁻³⁴. In their studies, the formation and shedding of the vortices due to VIM is
 7 clearly observed.

8
 9 A combined colinear wave-current interaction with four square columns platform is
 10 further studied experimentally^{35,36}. The findings indicated that the adding of wave
 11 sometimes tends to have little impact on VIM, while mitigating VIM entirely in other
 12 cases. This is further observed in the studies of Maximiano et al.³⁷ and Li et al.³⁸. A
 13 detailed examination on the fluid flow vorticity field indicated that the reduced
 14 amplitude of VIM is caused by the wave interaction with current and platform, changing
 15 the vortex shedding pattern, and thus the vortex shedding frequency.

16
 17 While VIM mitigation by waves is observed in past studies, most of existing
 18 investigations are focused on the flow condition where wave and current are aligned.
 19 In reality, it is very likely the angle between the wave and current can vary in different
 20 sea states. For instance, in the project of LIFE50+ for a 10MW wind turbine, the wave
 21 and current inter-angle ranges from 82.5 to 150 degrees at three deployment sites with
 22 a water depth over 50m³⁹. It is therefore critical to understand the wave-current-
 23 structure-interaction under various angles and flow conditions.

24
 25 In this paper, the dynamic response of the floating platform in complex sea conditions
 26 is numerically studied using a high-fidelity CFD tool⁴⁰. We aim at illustrating the
 27 underlying mechanisms that are related to the wave-current interaction with FOWT
 28 platforms using this tool. The rest of the paper is organized as follows. The numerical
 29 method including the governing equations of the fluid dynamics, the structural
 30 dynamics, and the mooring system, will firstly be presented in section II, together with
 31 a description of the physical problem to be studied and the parameters for both OC4
 32 DeepCwind platform by National Renewable Energy Laboratory (NREL) and the BW
 33 IDEOL platform with Électricité de France. Section III displays the numerical results,
 34 where the wave-only, current-only conditions are firstly examined for two FOWT
 35 platforms as comparisons. Then the combined wave-current condition studies for the
 36 OC4 platform at various wave-current angles and wave parameters are conducted, and
 37 the conclusions are drawn in the last section.

38 39 40 41 42 **II. PROBLEM STATEMENT**

41 The wave-current interaction of FOWT platform is simulated using an integrated
 42 toolbox based on OpenFOAM code. Particularly, the solver is a multiphase flow solver

1 interFoam in OpenFOAM. To apply mooring lines as restraints, an in-house code is
 2 integrated into interFoam. Additionally, a wave generation boundary condition and
 3 active wave absorbing scheme are implemented in the simulation⁶.

4 A. Numerical method

5 For a fluid problem, the Reynolds number $Re=UL/\nu$ is one non-dimensional parameter
 6 to differentiate between laminar and turbulent flows, where U is the fluid velocity, L is
 7 the characteristic length of the structure and ν is the kinematic viscosity. In this study,
 8 Re ranges from 8000 to 40000 for current-only cases, thus turbulence model is needed.
 9 The vortex shedding and the flow field surrounding structure are essential components
 10 in understanding VIM. As such, it's crucial to capture a precise structure of the vortex,
 11 a task which is normally not optimally accomplished by utilizing the standard
 12 Reynolds-Averaged Navier-Stokes (RANS) model due to its highly numerical
 13 dissipation. In this study, Large Eddy Simulation (LES) wall-adapted local eddy-
 14 viscosity (WALE) model⁴¹ is used. In LES, the largest, most energy-containing
 15 turbulent structures (large eddies) are explicitly resolved on the computational grid,
 16 while the smaller, more isotropic structures (small eddies or sub-grid scales) are
 17 modeled. The unsteady, incompressible Navier-Stokes equations are solved in LES
 18 model:
 19

$$20 \quad \frac{\partial \bar{u}_i}{\partial x_i} = 0 \quad (1)$$

$$21 \quad \frac{\partial \bar{u}_i}{\partial t} + (\bar{u}_j - u_g) \frac{\partial \bar{u}_i}{\partial x_j} = -\frac{1}{\rho} \frac{\partial \bar{p}}{\partial x_i} + \frac{\partial}{\partial x_j} \left[\nu \left(\frac{\partial \bar{u}_i}{\partial x_j} + \frac{\partial \bar{u}_j}{\partial x_i} \right) \right] - \frac{\partial \tau_{ij}}{\partial x_j} - g_i \quad (2)$$

22 where u_i is the velocity component in the i -direction, \bar{u}_i is the filtered velocity, u_g is
 23 the speed of the motion of the mesh grid. ρ is the density, p denotes dynamic pressure.
 24 g is gravity acceleration and t is the time. ν is the kinematic viscosity of the fluid and
 25 τ_{ij} is the subgrid-scale stress as following:

$$26 \quad \tau_{ij} = \bar{u}_i \bar{u}_j - \bar{u}_i \bar{u}_j \quad (3)$$

27 In order to capture the fluid motion at the air-water free surface, the Volume of Fluid
 28 (VOF) method⁴² is applied to solve the two-phase flow problem. The volume fraction
 29 (α) is governed by the following transport equation:

$$30 \quad \frac{\partial \alpha}{\partial t} + \nabla \cdot ((u - u_g)\alpha) + \nabla \cdot (u_r(1 - \alpha)\alpha) = 0 \quad (4)$$

31 To better capture an accurate interface, it is crucial to maintain a sharp interface and
 32 ensure that the α remains conservative and bounded between 0 and 1. To achieve this,
 33 OpenFOAM utilizes an artificial compression term $\nabla \cdot (u_r(1 - \alpha)\alpha)$, where u_r is a velocity
 34 field used to compress the interface and only functions near the free surface. For a
 35 water-air problem, fluid density and viscosity can be written as a mixture of water and
 36 air:

$$37 \quad \rho = \alpha \rho_w + (1 - \alpha) \rho_a \quad (5)$$

$$\mu = \alpha\mu_w + (1 - \alpha)\mu_a \quad (6)$$

where ρ_w and ρ_a denote the density of water and air, μ_w and μ_a denote their dynamic viscosity.

To generate numerical waves, the fluid velocity at the inlet boundary is prescribed using Stokes second-order wave theory:

$$u = \frac{\pi H}{T} \frac{\cosh k(z+d)}{\sinh kd} \cos \beta + \frac{3\pi H}{4T} \left(\frac{\pi H}{L} \right) \frac{\cosh 2k(z+d)}{\sinh^4 kd} \cos 2\beta \quad (7)$$

$$w = \frac{\pi H}{T} \frac{\sinh k(z+d)}{\sinh kd} \sin \beta + \frac{3\pi H}{4T} \left(\frac{\pi H}{L} \right) \frac{\sinh 2k(z+d)}{\sinh^4 kd} \sin 2\beta \quad (8)$$

where H and T denote the wave height and wave period, k and d denote wave number and water depth, β is the phase.

In this paper, to impose an non-reflection boundary conditions on the computational outlet boundary, an active wave absorbing scheme is utilized, with which the waves are directly absorbed along the boundary without relaxation zones⁴³. This can significantly reduce the computational domain size required by the relaxation zone^{6,44}. The primary concept is to produce waves with a phase opposite to that of the incident waves, but with the same characteristics at the outlet boundary. The corrected velocity at the outlet boundary is described by

$$\Delta u = -\Delta\eta \frac{\pi H}{T} \frac{\cosh k(z+d)}{\sinh kd} \quad (9)$$

where $\Delta\eta$ is the difference of the surface elevation η due to reflected waves. In this paper, two different models of moorings are utilized for two separate platforms. For the modeling of the spring-type mooring, it is simulated as a linear force proportional to the displacement:

$$f = k_s x \quad (10)$$

where k_s is the stiffness of the spring and x is the position of the center of rotation.

To model the catenary mooring lines constraining the platform, a quasi-static mooring line analysis model is utilized, in which a mooring line is treated as multiple segments with identical length⁴⁵. For each segment, equations of static equilibrium are established in both horizontal and vertical directions, which can be illustrated in Figure 1. The equilibrium equations are:

$$T_{x(i+1)} = T_i, \quad T_{z(i+1)} = T_{iz} + w_i dl \quad (11)$$

where T is the tension and w_i is the unit weight of each segment. To consider the extension of the mooring lines, each segment should be subjected to the following geometric constraints:

1
$$ds \cos(\varphi_{i+1}) = x'_i + x'_{i+1} = \bar{x}$$
 (12)

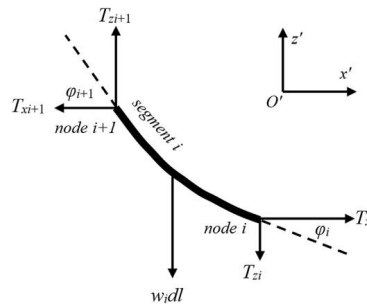
2
$$ds \sin(\varphi_{i+1}) = z'_{i+1} + z'_i = \bar{z}$$
 (13)

3 where ds is the stretch length of the segment, E and A denote Young's modulus and
4 cross-sectional area for the segment, respectively.

5 Although the mooring lines are not directly simulated using CFD, the hydrodynamic
6 forces are estimated by using Morison's equation. The fluid information is derived from
7 the field information from the CFD background mesh at the corresponding positions.
8 The dynamic response of the platform is governed by the following motion equations:

9
$$m\ddot{x} + c\dot{x} + kx = F_x \quad \text{and} \quad m\ddot{y} + c\dot{y} + ky = F_y$$
 (14)

10



11

12

13

14

15

16

17

18

19

20

21

22

23

24

25

26

27

28

29

30

31

32

33

34

35

36

37

38

39

40

Figure 1. Sketch of the segment in the mooring line analysis model

where m , c and k represent the platform mass, structural damping coefficient, and spring stiffness, respectively. F_x and F_y denote the IL and CF hydrodynamic force acting on the platform. The Newmark-beta method is adopted to solve Eq. (13) for the motion of the platform. To ensure simulation stable, an acceleration relaxation factor of 0.9 is adopted. Since we focus on the IL and CF motion of the platform, only x and y degrees of freedom are considered.

B. Model description

The two platforms studied are OC4 semi-submersible platform and a barge IDEOL platform as shown in Figure 2. The OC4 semi-submersible platform model is based on a 1:73 model test performed at the University of Tokyo by Gonçalves et al²⁶. The platform is made up of four columns, one central column with a smaller diameter and three offset columns with larger diameters. Columns are connected by crossbars in between. There are base columns attached below the side columns. In the experiment, the model was restrained by four perpendicular mooring lines. The main parameters, including the equivalent stiffness of the mooring system, are summarised in Table 1.

This is the author's peer reviewed, accepted manuscript. However, the online version of record will be different from this version once it has been copyedited and typeset.

PLEASE CITE THIS ARTICLE AS DOI: 10.1063/5.0158917

Accepted to Phys. Fluids 10.1063/5.0158917

1 The natural frequencies of the platform in IL and CF directions are 9.4s and 9.6s,
2 respectively, which were obtained via free decay tests.

3
4 The barge IDEOL platform is a 1:50 model, which was experimentally tested in the
5 National Research Institute of Fisheries Engineering (NRIFE) wave tank in Japan⁴⁶,
6 shown in Figure 2(b). The width of the barge semi-submersible platform is 0.82m, with
7 a draught of 0.14m. The skirt with 0.055m width is attached at the bottom to reduce the
8 dynamics motion response. Compared to the OC4 platform, this barge platform has a
9 simpler geometry and is easier to construct, with a larger area of water plane and smaller
10 draft. To constrain the platform, three catenary mooring lines are applied. The nominal
11 diameter of these studless chains is 3mm with a total length of 8m. The geometric
12 parameters of the platform can be found in Figure 2 and Table 1.

13
14 In ocean engineering, the geometry of a platform significantly influences its motion
15 response, particularly in interaction with water currents. The above two platforms
16 exhibit distinct geometries, primarily differentiated by their waterplane (WP) area. The
17 IDEOL barge platform, akin to a hollowed-out box, has a substantially larger WP area
18 compared to the SS platform. This expands WP area results in a shallower draft and a
19 reduced aspect ratio (defined as draft/characteristic length). In a vortex-induced motion
20 (VIM) study, a lower aspect ratio typically exhibits enhanced three-dimensional
21 characteristics at the platform's bottom edge, subsequently altering the motion
22 amplitude.

OC4 Platform		IDEOL Platform	
Central column diameter	$D_c=0.09\text{m}$	Thickness of Skirt plate	$d_s=0.004\text{m}$
Offset Column diameter	$D_o=0.165\text{m}$	Skirt plate width	$W_s=0.055\text{m}$
Base column diameter	$D_B=0.33\text{m}$	Width	$W_B=0.82\text{m}$
Height of base column	$d_B=0.083\text{m}$	Height	$H_B=0.19\text{m}$
Platform draft	$d=0.27\text{m}$	Platform draft	$d=0.14\text{m}$
Distance between offset columns	$L=0.688\text{m}$		
Inertia properties			
Mass of the Platform	$m=36.7\text{kg}$	Mass of the Platform	$m=62.31\text{kg}$
Centre of mass	$z_c=-0.134\text{m}$	Centre of mass	$z_c=0.03\text{m}$
Mooring parameters			
Stiffness in x direction	$k_x=27.5\text{N/m}$	Type	Studless
Stiffness in y direction	$k_y=28.1\text{N/m}$	Weight in water	0.067kg/m

Table 1. Geometric parameters and the mooring parameters

This is the author's peer reviewed, accepted manuscript. However, the online version of record will be different from this version once it has been copyedited and typeset.

PLEASE CITE THIS ARTICLE AS DOI: 10.1063/5.0158917

Accepted to Phys. Fluids 10.1063/5.0158917

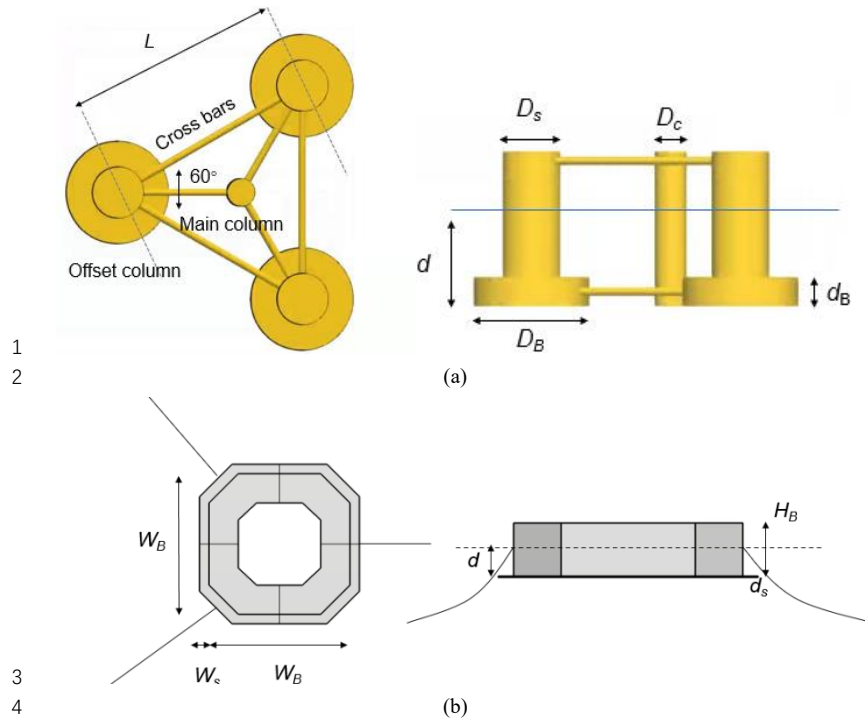


Figure 2. Sketch of the scale-down model for (a) OC4 Platform (b) IDEOL platform

C. CFD settings

The computational domain is shown in Figure 3 with top and side views. The boundary conditions are set as follows: the zero-gradient pressure condition is applied at the inlet and outlet boundaries with the air speed equal to zero, while the fluid velocity are given by a build-in boundary based on the wave theory, for the generation of inflow wave-current condition and wave absorbing. For those cases with oblique incident waves, the front boundary is imposed the same settings as the inlet boundary condition for wave generating. A non-slip wall boundary condition is applied to the bottom.

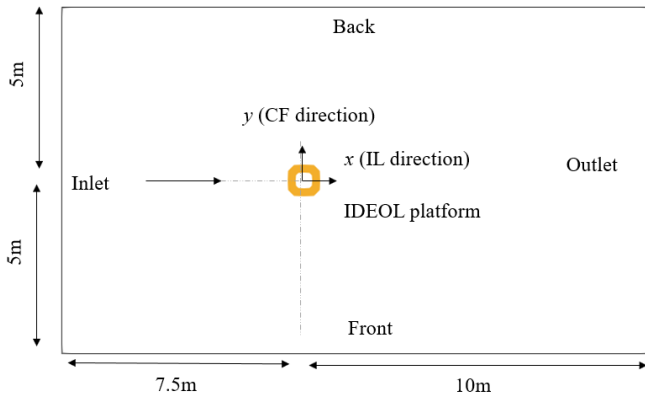
This is the author's peer reviewed, accepted manuscript. However, the online version of record will be different from this version once it has been copyedited and typeset.

PLEASE CITE THIS ARTICLE AS DOI: 10.1063/5.0158917

Accepted to Phys. Fluids 10.1063/5.0158917

1

2



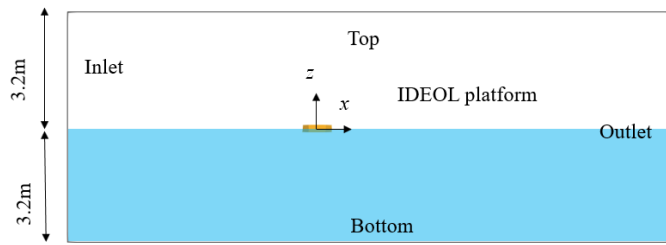
(a) Top view

3

4

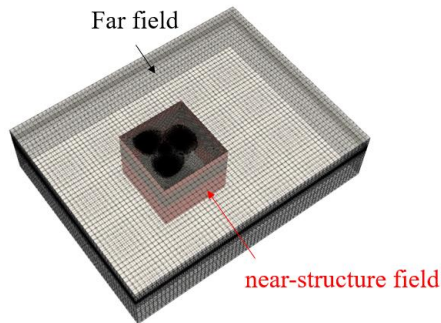
5

6



(b) Side view

Figure 3. (a)Top view (b)Side view of the numerical wave tank for IDEOL platform



7

8

9

10

Figure 4. Computational mesh for the OC4 platform, the inner red zone is structured mesh to capture boundary layers with high quality, outside which is the unstructured far-field mesh, where the mesh is only refined near the water-air surface.

1
2
3
4
5
6
7
8
9
10
11
12
13
14
15
16
17
18
19
20
21
22
23
24
25
26

To accurately model the motion of platform under both wave and current conditions, it is essential to ensure that the mesh resolution meets different mesh density requirements. For instance, to capture VIM, the separation of the boundary layer around the structure and the vortex street at the downstream should be accurately modelled. Therefore, CFD mesh is refined at the near wall field region as well as the wake region. To reduce the overall cell numbers of the computational domain, a hybrid mesh is used, which is made up of the near-field structured mesh (red one) and the far-field unstructured mesh as shown in Figure 4. Within the boundary layer, the thickness of the mesh is set that the y^+ around the platforms ranges from 1.0 to 4.0. The surface cell on the platform is $1/100$ of the characteristic length D . At the near field of the structure, the average cell size is $1/50D$. At the far field region, to ensure the accuracy of numerical wave generation, the cells near air-water free surface are refined. In particular, at least 8 cells are used along z direction per wave height, and at least 180 cells per wavelength.

The convergence test of the numerical simulation is conducted, and the results are shown in Table 2. Three mesh sets with different cell counts are used, with which the normalized IL and CF motion (A_x/D and A_y/D) are compared, as well as the frequency of the cross-flow oscillation f/f_n . The disparity between the Medium and Fine cases is less significant than that between the intermediate and coarse cases. This suggests that the intermediate grid is sufficient fine for the current research. Similarly, for the sensitivity study with different time steps, the predicted motion hardly changes when $U\Delta t/D < 0.002$. Considering the cost of computational time, a time step of $U\Delta t/D = 0.002$ is chosen for the CFD modelling in this study.

Mesh	Cell count	$U\Delta t/D$	A_x/D	A_y/D	f/f_n
Coarse	2,650k	0.002	0.050	0.424	0.990
		0.001	0.055	0.403	0.959
Intermediate	3,510k	0.002	0.059	0.410	0.958
		0.004	0.077	0.421	0.932
Fine	5,400k	0.002	0.061	0.402	0.959

Table 2. Sensitivity study for computational mesh and unsteady time step for OC4 platform with $V_r = 8.1$

PIMPLE (a combination of Pressure Implicit with Splitting of Operator (PISO) and Semi-Implicit Method for Pressure-Linked Equations (SIMPLE)) algorithm is utilized to solve the pressure-velocity coupling. A second-order Crank-Nicolson scheme is used for temporal discretization. Second-order upwind scheme is adopted for convective terms. Gradient terms are handled via a second-order cell-limited Gauss linear scheme. The total cell of the simulation is around 350 million for both platforms. The

1 computations are made in parallel with 5 nodes (180 cores) for each case on Cirrus HPC
 2 (<http://www.cirrus.ac.uk>). The average simulation time is $3T_n$ per day which may vary
 3 depending on the specific cases.
 4

5 III. Results & Discussions

6
 7 When waves and currents coexist, their respective motions become coupled. To
 8 decouple this effect, we start with a comparative study on a fluid-structure-interaction
 9 either induced by wave or current separately for both OC4 and IDEOL platforms.
 10 Because of their different geometric characteristics, it is expected to observe different
 11 dynamic motion response. For the validation purpose, the comparison between our
 12 CFD results with experimental testing has been done for waves interaction with IDEOL
 13 platform. Other validations for this CFD tool can be found from our previous
 14 publications on (a) wave-structure interaction for floating platforms^{8, 47}, (b) wave
 15 energy devices⁴⁸, and (c) the current-structure interaction for the OC4 platform with
 16 VIM studies^{49, 50}.
 17

18 A. Response of the OC4 Platform with Current-only and Wave-only conditions

19
 20 Either current or wave interaction with OC4 platform is firstly studied and the flow
 21 conditions are listed in Table 3. Figure 5 displays the amplitude of the motion response
 22 in the current-only scenario along with the experimental data, in which IL component
 23 (A_{cx}) and CF component (A_{cy}) are plotted against flow velocities. They are calculated
 24 by multiplying the root mean square (RMS) displacement by $\sqrt{2}$, and then normalized
 25 with the characteristic length, which is D_s for OC4 platform and W_B for IDEOL platform.
 26
 27
 28

Wave Parameters

H [m]	0.02	0.04	0.07	0.09	0.116	T [s]	1.5	2.0	2.63
Scaled 1:73						Scaled 1:73			
H [m] Full-scale	1.45	2.91	5.09	6.54	8.44	T [s]	12.78	17.04	22.4
						Full-Scale			

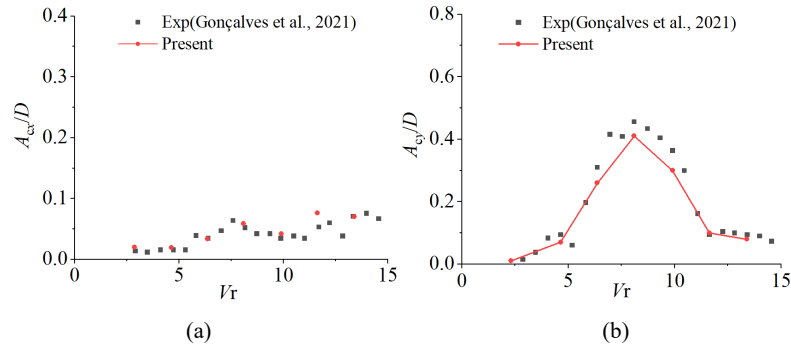
Current parameters

U [m/s]	0.05	0.08	0.11	0.14	0.17	0.20	0.24
Scaled 1:73							
U [m/s]	0.43	0.68	0.94	1.20	1.45	1.70	2.05
Full-scale							
V_r	2.30	3.7	4.6	8.1	9.9	11.6	14.3

Table 3. Wave and current parameters for OC4 Platform testing

1 In VIM analysis, the freestream velocity is commonly normalized using the natural
 2 frequency of the system (f_n). The reduced velocity is defined as $V_r = U/f_n D$, where U and
 3 D are the flow velocity and characteristic length of the structure. It can be re-written as
 4 $V_r = UT_w/D$, where T_w is the natural frequency of structure. From a physical perspective,
 5 the numerator can be considered as the distance that the constant fluid flows over the
 6 structure in one natural vibration period. Thus, V_r is an indicator for the ratio between
 7 this distance and the structural dimension. In this study, cases with different V_r are
 8 achieved by only varying the flow velocity, meanwhile Re number is also synchronized
 9 with V_r since they are both a representative of the flow velocity.

10
 11 The plot indicates that the CFD predictions are in good agreement with the experiments.
 12 The IL motion is significantly smaller compared to that of CF motion with A_{cy}/D being
 13 less than 0.1, indicating that the IL movement of platform is not dominant. The CF
 14 motion response shown in Figure 5(b), however, reveals a very typical current-
 15 structure-interaction VIM phenomenon. In particular, the lock-in region ranges from V_r
 16 =5 to 10, in which the maximum A_{cy}/D characterized by VIM reaches a value of 0.41
 17 at $V_r = 8.1$. At real sea conditions, the full-scale current velocity in the lock-in region
 18 can vary from 1.0 to 1.45 m/s. Therefore, it is expected to observe significant platform
 19 motion within this velocity range.
 20



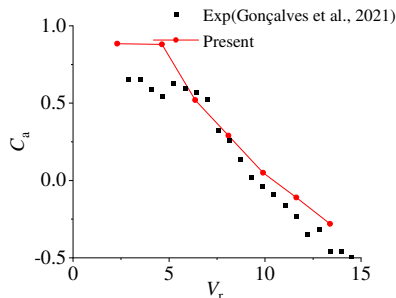
21
 22
 23 Figure 5. Variation of the motion response amplitude with V_r in (a) IL direction and (b)
 24 CF direction for OC4 platform with current-only condition
 25

26 The added mass coefficient in the CF direction (C_a) also agrees well with the
 27 experiment as shown in Figure 6, which is defined as $C_a = -R \left\{ \frac{fft[F_y(t)]}{fft[y(t)]} \right\} / m$ where $F_y(t)$,
 28 y are the hydrodynamic force and displacement in CF direction, respectively. $R()$
 29 represents the real part of the complex number and fft represents Fast-Fourier Transform
 30 (FFT) operator. The large and positive values of C_a with $V_r < 9.9$ denote the
 31 synchronization with the vortex shedding frequency. As the velocity increases, C_a
 32 decreases and becomes negative after $V_r > 9.9$, indicating the end of resonance.
 33

This is the author's peer reviewed, accepted manuscript. However, the online version of record will be different from this version once it has been copyedited and typeset.

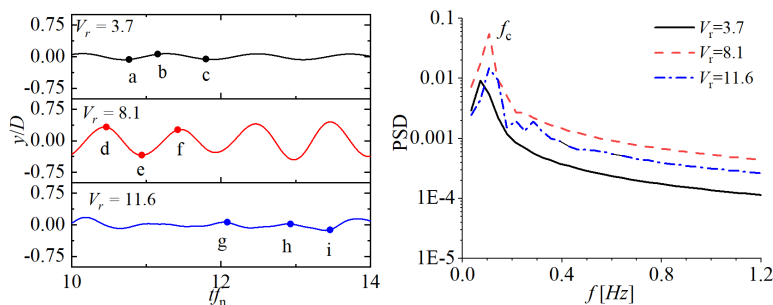
PLEASE CITE THIS ARTICLE AS DOI: 10.1063/5.0158917

Accepted to Phys. Fluids 10.1063/5.0158917



1
2
3
4

Figure 6. Variation of added mass coefficient with V_r in CF direction for OC4 platform with current-only condition



5
6
7
8

Figure 7. Time-series and FFT analysis of CF motion response for $V_r = 3.7, 8.1$ and 11.6 for OC4 platform with current-only condition

9 The resonance in lock-in region is also reflected by the time-series and the
10 corresponding FFT analysis shown in Figure 7, where a dominant VIM motion can be
11 observed at $V_r = 8.1$ in lock-in region. With a smaller $V_r = 3.7$, the periodic motion
12 exists but has a lower frequency and smaller amplitude. At larger V_r beyond lock-in
13 region, the amplitude is small but with higher-order frequency components.

14
15 The vorticity field is plotted and examined in Figure 8 to reflect the typical vortex
16 shedding associated with VIM phenomenon. It is seen that with the increase of V_r ,
17 the vorticity becomes stronger, and the flow field becomes more irregular. Within the lock-
18 in region at $V_r = 8.1$, (Figure 8(d)-(f)), the vortices generate alternately from both
19 sides of column, and then shed from either side of the column at a frequency equal to the
20

This is the author's peer reviewed, accepted manuscript. However, the online version of record will be different from this version once it has been copyedited and typeset.

PLEASE CITE THIS ARTICLE AS DOI: 10.1063/5.0158917

Accepted to Phys. Fluids 10.1063/5.0158917

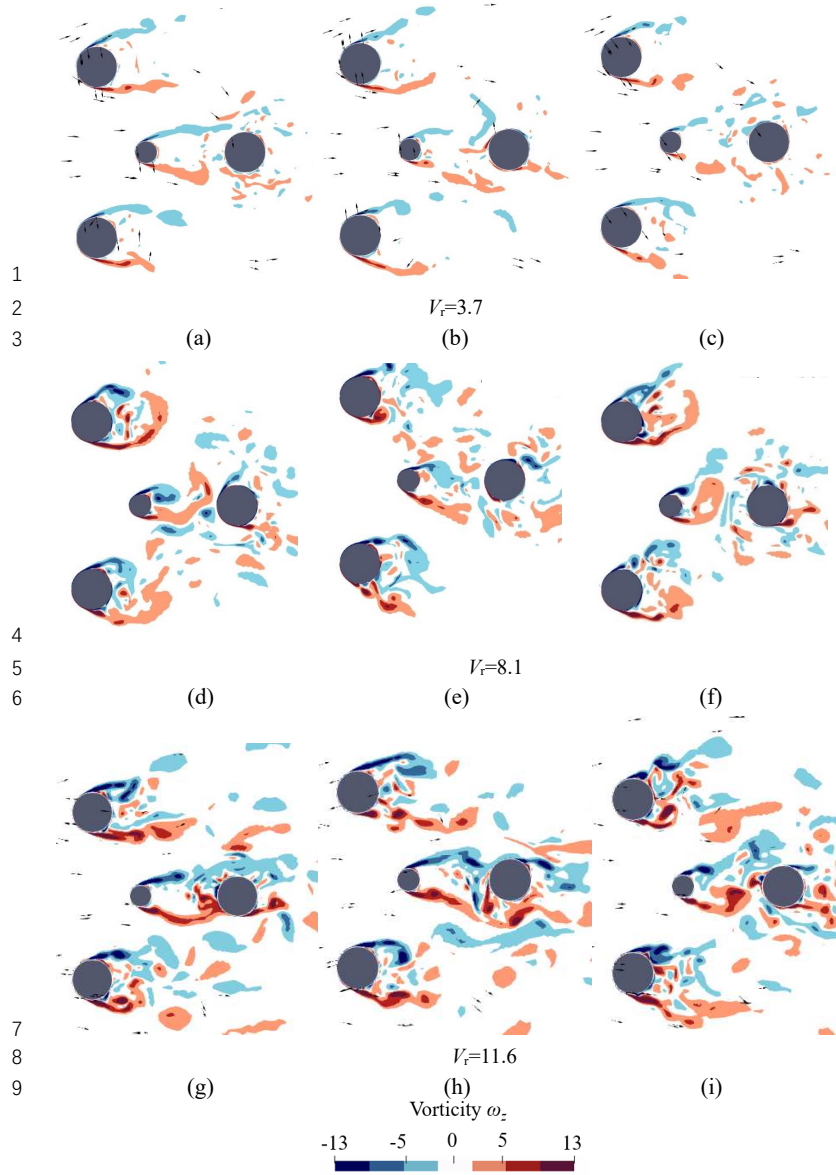


Figure 8. Contours of spanwise vorticity ω_z at the section with $z = -0.1\text{m}$ at the time instants shown in Figure 7 at $V_i = 3.7$ (a)-(c), $V_i = 8.1$ (d)-(f) $V_i = 11.6$ (g)-(i) for OC4 platform with current-only condition.

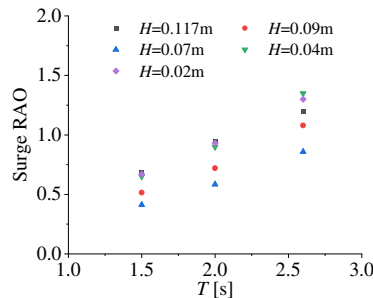


Figure 9. Variation of surge RAOs with wave periods of OC4 platform for wave-only condition

lock-in frequency f_n . An anti-clockwise vortex is observed when the platform reaches y_{\min} in Figure 7 (e), and another anti-clockwise vortex is observed while a clockwise vortex is shed when y_{\max} at (f), revealing a typical 2P mode for the wake in VIM. At $V_r = 3.7$, no obvious vortex shedding is observed, which associates with a smaller motion in CF direction.

In addition to the above current-only condition, the wave-only condition is also examined for OC4 to set up a baseline model for the subsequent wave-current investigations. Figure 9 shows the predicted surge RAO with various wave heights (H) and wave periods (T). It is seen that the RAO increases with T , as the platform's structure natural period aligns more closely with it, increasing the motion response. The RAO relationship with H is rather complex due to enhanced mooring forces with increasing H , as well as the higher nonlinearity with larger H . Therefore, the variation follows a nonlinear trend.

B. Response of the IDEOL Platform with Current-only and Wave-only conditions

The IDEOL platform is analysed starting with the current-only scenarios. The response amplitudes in IL and CF directions are shown in Figure 10, with the parameters summarised in Table 4. It is seen that, barge-type platform has an even smaller IL motion compared with OC4 platform. The motion in CF direction is also relatively smaller. For the largest reduced velocity of $V_r=9.6$ ($U=2.3$ m/s at full-scale), the maximum A_{cy}/D is less than 0.2. Only at this largest V_r , the periodic platform motion characterized by VIM becomes notable, as shown in the time-series plots in Figure 11.

Compared to OC4 platform, the VIM phenomena are less profound, which might be due to several reasons.

This is the author's peer reviewed, accepted manuscript. However, the online version of record will be different from this version once it has been copyedited and typeset.

PLEASE CITE THIS ARTICLE AS DOI: 10.1063/5.0158917

Accepted to Phys. Fluids 10.1063/5.0158917

1 Firstly, the most pronounced Vortex Induced Motion (VIM) for the SS platform occurs
 2 around $V_r=8.1$. Comparatively, for the IDEOL platform to experience significant VIM,
 3 it requires a much higher reduced velocity of at least 10.0 or even higher, as can be seen
 4 in Figure 10. Thus, the VIM of IDEOL platform is not obvious. In addition, the aspect
 5 ratio of IDEOL platform is 0.17, which is much smaller than that of 1.64 for OC4
 6 platform. This finding agrees with the research by Goncalves et al. that the response of
 7 CF motion of a cylinder weakens as its aspect ratio decreases. The VIM could be even
 8 negligible if the aspect ratio is less than 0.3¹⁸.

Wave parameters					Current parameters			
T [s]	1.6	1.8	2	2.2	U [m/s] Scaled 1:50	0.20	0.26	0.32
Scaled 1:50					U [m/s] Full-scale	1.4	1.8	2.3
T [s]	11.3	12.7	14.1	15.6	V_r	6.1	8.0	9.6
Full-Scale								

Table 4. Wave and current parameters for IDEOL platform testing

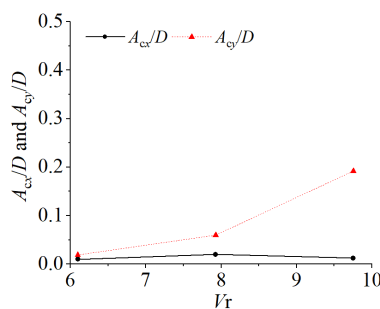


Figure 10. CF and IL motion amplitude versus reduced velocity for IDEOL platform with current-only condition

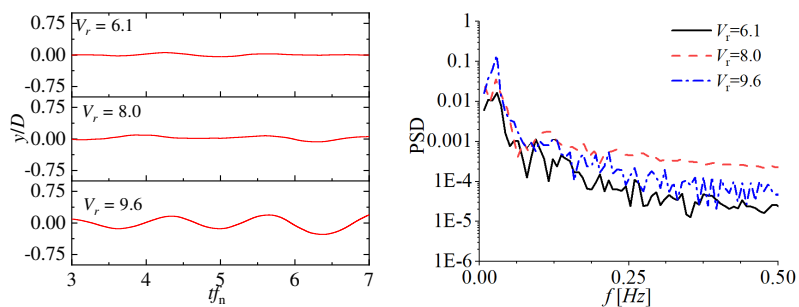


Figure 11. Time-series and FFT analysis of CF motion response for $V_r = 6.1, 8.0$ and 9.6 for IDEOL platform with current-only condition

This is the author's peer reviewed, accepted manuscript. However, the online version of record will be different from this version once it has been copyedited and typeset.

PLEASE CITE THIS ARTICLE AS DOI: 10.1063/5.0158917

Accepted to Phys. Fluids 10.1063/5.0158917

1 Then, the dynamic response of IDEOL platform for wave-only condition is studied for
 2 a series of wave periods (Table 4). In the experiment, the wave heights varied from
 3 2.5m to 7.5m. In this validation, an intermediate wave height of $H=5\text{m}$ is chosen. Figure
 4 12 shows the predicted RAOs in comparison with the experiment (EXP) and numerical
 5 modelling (SIM) data. In the SIM studies, the potential-flow-based method is used, the
 6 hydrodynamic coefficient is obtained by Ansys Aqwa software and the dynamic
 7 response is calculated using DNV-GL's Bladed software package⁴⁶ to couple the
 8 hydrodynamic loads. The RAOs are normalized by the wave amplitude for heave and
 9 surge motions, while the pitch response is normalised by $kH/2$ Figure 12.

10

11

12

13

14

15

16

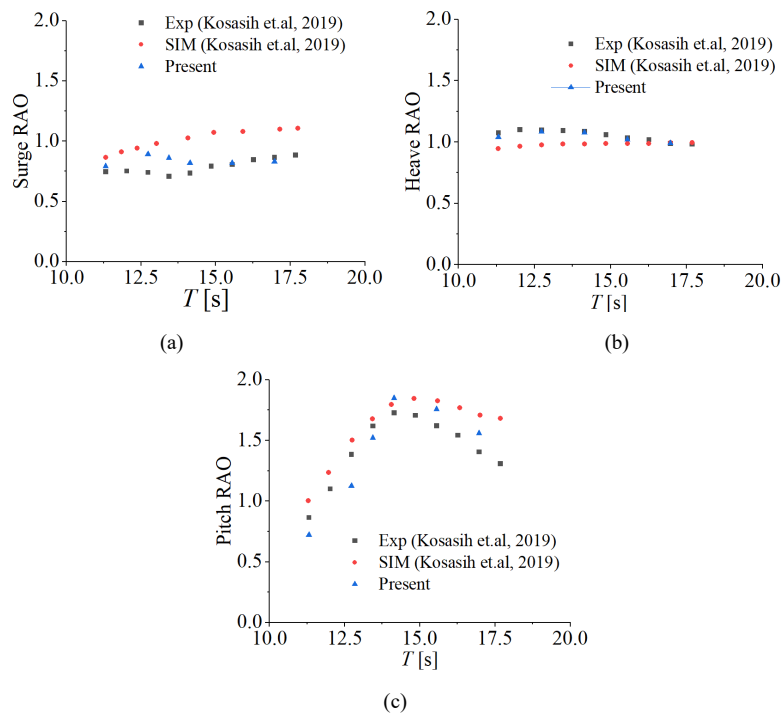


Figure 12. Variation of RAOs with wave periods with $H=5\text{m}$ for (a) surge (b) pitch (c) heave for IDEOL platform with wave-only condition

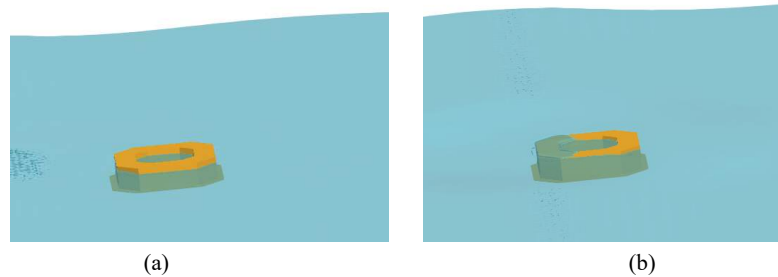


Figure 13. Wetted surface changes on the IDEOL platform at different sampling time (a) $t/T=3.5$ and (b) $t/T=4.0$ with $H=5\text{m}$ and $T=14.1\text{s}$

For the wave periods studied, an averaged RAO for the surge and heave are typically 0.84 and 1.0, respectively, from CFD and EXP. However, the pitch RAO reveals an initial increasing and then decreasing trend. The peak RAO occurs at $T=14.1\text{s}$. It is evident that better agreement between the present CFD predictions and the experimental data has been reached than the results obtained from the potential-flow-based tool (SIM). One explanation for the improved accuracy of CFD modelling over the potential theory method is that the later linearizes the wave-air free-surface equation at the time-averaged positions, therefore, the nonlinear effect of fluid-structure interaction, represented by the changing wetted surfaces, is not very well captured⁴⁶. As shown in Figure 13, the green water can be observed clearly showing the changing wetted surface. Also, for the CFD modelling, tuning the viscous damping to fit the experiments is not required which is usually needed for a viscous-modified potential flow model.

C. Response with combined current-wave at different angles

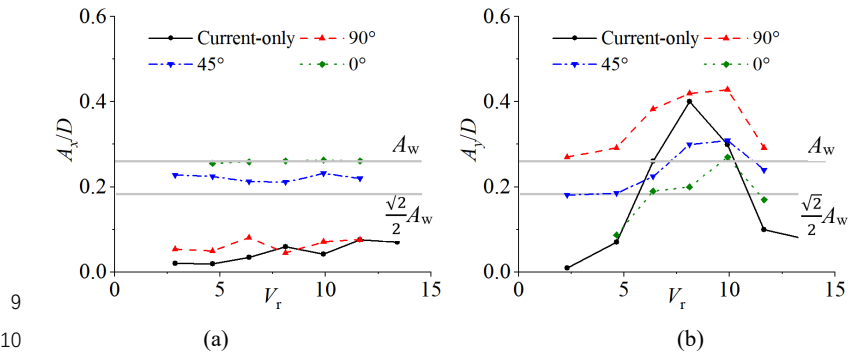
In the above two sections for current-only and wave-only cases, it is observed that the VIM phenomena are more profound for a semi-submersible platform than a barge platform. Therefore, the following studies on a combined wave-current-structure interaction will be focused on OC4 semi-submersible platform.

It is well known that in a real sea state, current and wave do not always exist alone, and the extreme loading condition for a FOWT platform may occur with specific combinations of wave and current. In our previous study on a colinear wave-current condition³⁸, it was found that the current-induced CF motion can be mitigated with the addition of waves, depending on V_c under investigation. This conclusion is consistent with others' findings. Some other studies also found that if the wave and current were non-colinear, the mitigation became less obvious^{51, 52}. To investigate this phenomena, this section is dedicated to examining the impact of the angle of the flow direction between current and wave (θ) on the platform's dynamic responses. Three angles varying from $\theta=0^\circ$ to 90° are selected. Typical wave period and wave height are $T=2.0\text{s}$,

1 $H=0.09\text{m}$. The current speed varies from 0.05 to 0.20 m/s, leading to the reduced
 2 velocity V_r ranging from 2.3 to 11.6, as shown in Table 5.
 3
 4

U [m/s]	0.05	0.08	0.11	0.14	0.17	0.20
Scaled 1:73						
U [m/s]	0.43	0.68	0.94	1.20	1.45	1.70
Full-scale						
V_r	2.30	3.7	4.6	8.1	9.9	11.6

5
 6 Table 5. Current parameters for wave-current interaction with OC4 platform on the
 7 effect of angles
 8



11

12

13

14

15

16

17

18

19

20

21

22

23

24

25

26

27

28

29

30

31

32

33

34

35

36

37

38

39

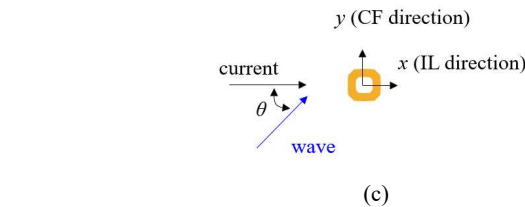


Figure 14. Variation of motion response in wave-current condition with V_r and θ ($H=0.09\text{m}$ and $T=2.0\text{s}$) (a) IL direction and (b) CF direction (c) is the sketch of the direction of current and wave. The horizontal line (A_w) is the amplitude of current and wave. The horizontal line (A_w) is the amplitude shown in Figure 9 for wave-only test, and $\sqrt{2}/2A_w$ denotes the motion components at $\theta=45^\circ$

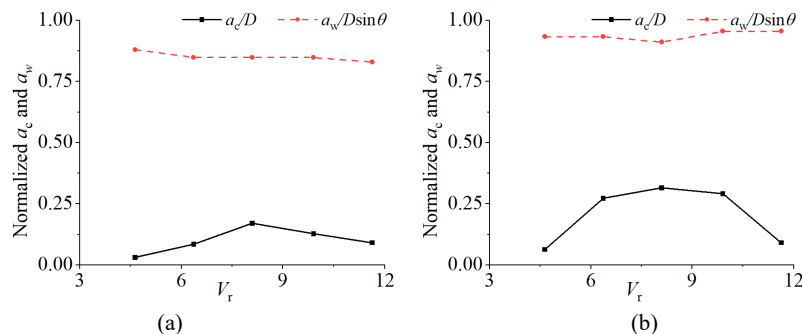
The responses of platform are shown in Figure 14 with different angles. Given a combined wave-current condition, the IL motion varies a little with reduced velocity, indicating that varying current speed does not affect IL motion significantly, as shown in Figure 14 (a). However, the IL motion is noticeably impacted by angles variation (θ). In fact, with $\theta = 0^\circ$, A_x/D is the largest and close to A_w in the wave-only cases, while $\theta = 90^\circ$, A_x/D is the smallest and close to that in the current-only cases. Unlike the above

1 IL response, CF motion varies significantly with reduced velocity and the peak values
 2 can be clearly captured (Figure 14 (b)). As the angle θ increases, A_y/D increases across
 3 all V_r . Therefore, for safety design purposes, it is recommended to pay more attention
 4 to those cases with $\theta = 90^\circ$. Beyond the lock-in region, with $\theta > 0^\circ$, A_y/D are greater than
 5 those observed in the current-only cases, and close to A_w . However, within lock-in
 6 region, with increasing θ to 90° , A_y/D is always larger than that of either wave-only or
 7 current-only. The large CF motion in this wave-current condition is induced by non-
 8 zero wave-current angle. As the velocity components along y -axis increase with the
 9 angle, CF response increases due to the enlarged inertia wave force acting on the
 10 platform. In addition, the flow field and VIM are altered with a combined wave-current
 11 interaction.

12
 13 To examine the individual effect of current and wave on the motion response, the above
 14 CF motion (A_y/D) is decomposed:

$$a_c = |Y(f_c)| \quad \text{and} \quad a_w = |Y(f_w)| \quad (15)$$

15
 16 where $|Y(f)|$ is the FFT of CF motion. a_c and a_w are the motion amplitudes induced by
 17 current and wave, f_c and f_w are the peak frequency corresponding to VIM and the wave.
 18 The decomposed a_w and a_c for $\theta = 45^\circ$ and 90° are shown in Figure 15 (a) and (b). For
 19 both angles, a_w almost remain unchanged with V_r . As a result, the contribution of wave
 20 to the total response is nearly constant with varying V_r .



22
 23
 24 Figure 15. Variation of decomposed CF motion excited by current (a_c) and waves (a_w)
 25 ($H=0.09\text{m}$ and $T=2.0\text{s}$) at angles of (a) 45° and (b) 90° , a_c is normalized by
 26 characteristic dimension D and a_w is normalized by wave amplitude multiplied by
 27 $\sin(\theta)$

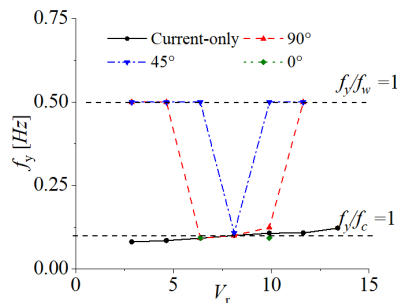


Figure 16. Variation of dominant frequency with V_r ($H=0.09\text{m}$ and $T=2.0\text{s}$)

However, the variation of a_c with V_r resembles the pattern of current-only cases, with the peak amplitude occurring at $V_r=8.1$ and decreasing beyond this V_r . This indicates that the VIM effect still exists even with waves. Hence, the response peaks in the wave-current cases depicted in Figure 14 are primarily due to the current's contribution within lock-in region. A comparison between Figure 15 (a) and (b) indicates that larger θ leads to an amplified VIM. It is also worthwhile to note that with a larger angle, the a_c near the peak value at $V_r=8.1$ also increases, which means the VIM becomes significant for a wider range of reduced velocities with the addition of waves.

The effects of angle are also reflected in dominant frequencies, as analysed in Figure 16. For current-only cases, f_y increases with V_r , locks onto f_c in lock-in region, leading to a large motion response. For cases with $\theta=0^\circ$, f_y is the same as that of current-only. However, for those with $0^\circ < \theta < 90^\circ$, outside lock-in region, f_y is close to f_w indicating the platform's motion is dominated by waves. Within lock-in region $f_y=f_c$, the resonance occurs. With an increasing θ , the lock-in region becomes wider, revealing a more vulnerable platform due to large-scale motions under a wide range of current velocity. The time-series distribution of y/D and their FFT analysis displayed in Figure 17 reinforce the above observations. In fact, two dominant frequencies appear in relation to f_c and f_w . Outside lock-in region, the low-frequency components are not as prominent compared to the high-frequency components. Within lock-in region, the low-frequency component is substantially large and increases with angles. In addition to the above dominant frequencies, other spikes are also noted, which might be caused by the nonlinear coupling between the vibration of platform and fluid flow. The difference frequency $f_{\text{diff}}=f_w - f_c$ and sum frequency $f_{\text{sum}}=f_w + f_c$ exist, although with a relatively small magnitude, which is also noticeable in the cases with 90° with their magnitudes increasing with angle.

This is the author's peer reviewed, accepted manuscript. However, the online version of record will be different from this version once it has been copyedited and typeset.

PLEASE CITE THIS ARTICLE AS DOI: 10.1063/5.0158917

Accepted to Phys. Fluids 10.1063/5.0158917

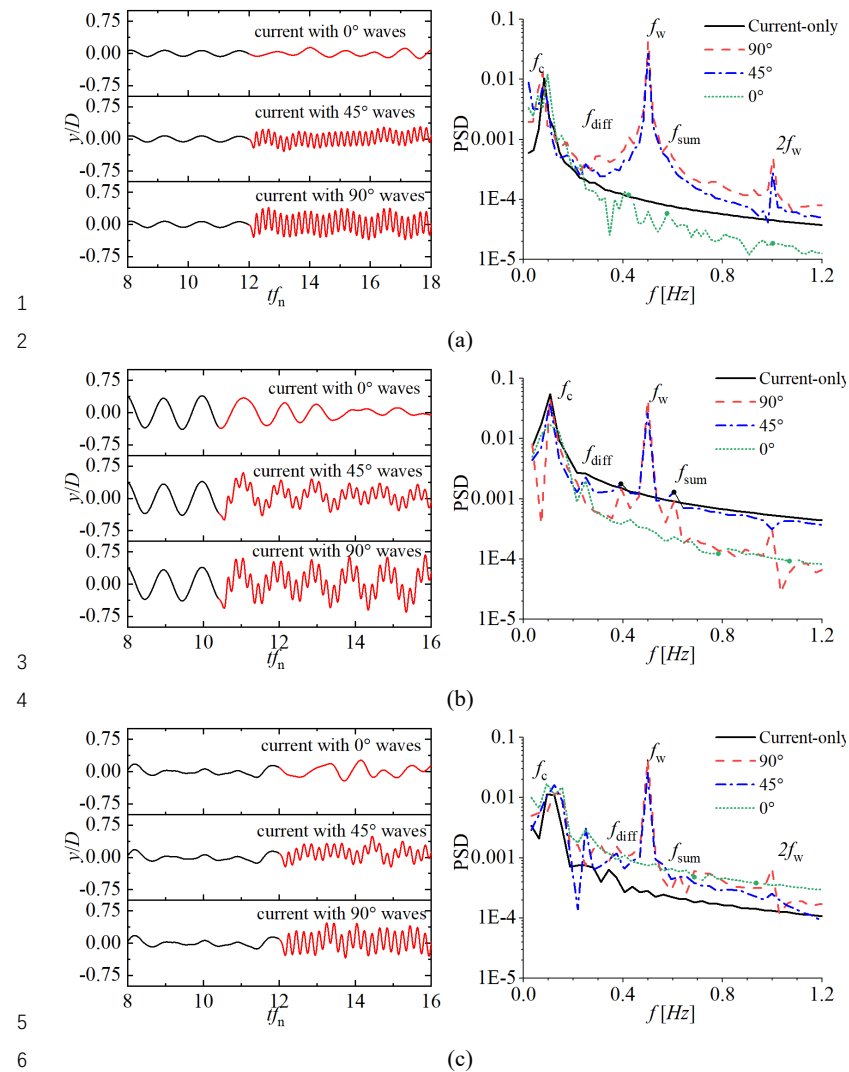


Figure 17. Time-series and FFT analysis of CF motion response in wave-current condition ($H=0.09\text{m}$ and $T=2.0\text{s}$) of (a) $V_r=4.6$ (b) $V_r=8.1$ (c) $V_r=11.6$. In the time-series, black line represents the response caused by the current only, while red line indicates the addition of waves to the current.

This is the author's peer reviewed, accepted manuscript. However, the online version of record will be different from this version once it has been copyedited and typeset.

PLEASE CITE THIS ARTICLE AS DOI: 10.1063/5.0158917

Accepted to Phys. Fluids 10.1063/5.0158917

1 Figure 18 to Figure 19 present vorticity field under the combined waves and current
 2 conditions for $\theta=0^\circ$ and $\theta=90^\circ$ at $V_i=8.1$. Unlike the current-only cases in Figure 8, the
 3 fluid field with waves for $\theta=0^\circ$ in Figure 18 becomes chaotic and its precise pattern is
 4 hard to discern. It displays the characteristics of cylindrical structures interacting with
 5 both steady and oscillatory flow. The steady flow leads to a typical VIV vortex shedding,
 6 while the oscillatory flow leads to a different shedding pattern. The specific appearance
 7 of pattern highly relies on the Keulegan-Carpenter number (KC number)⁵³, which
 8 describes the relative importance of the drag forces over inertia forces in an oscillatory
 9 flow. In a pure oscillatory flow scenario, VIM only occurs at a large KC , by the
 10 hydrodynamic lift force in CF direction

$$11 \quad KC = \frac{U_M}{f_w D} \quad (16)$$

12 where U_M is the maximum flow velocity in the IL direction. At time instants of (c) to
 13 (e), the vortices are shed from both sides of offset columns (the larger columns) and
 14 move downstream, having a symmetric pattern. The vortex shedding frequency of this
 15 process is 1/2 seconds, much smaller than lock-in frequency, but is identical to the wave
 16 frequency f_w , indicating that the symmetric vortex pair is dominated by oscillatory
 17 flow/waves. When oscillatory flow passed a cylinder at a small KC number between
 18 1.6-4.0, the vortex separation begins to occur in the form of a pair of symmetric attached
 19 vortices¹⁶, as also observed for offset column with $KC=2.1$. Two vortex pairs generate
 20 in one cycle, one from the previous half period where flow passes in one direction.
 21 Another pair generate from the second half period when the oscillatory direction
 22 reverses. In the present case for wave-steady current, only one vortex pair generates
 23 within one cycle and is flushed downstream, showing a 2T mode (Figure 18(b)), where
 24 three vortices are seen to be shed from the lower offset column. This mode was also
 25 observed in Zhao's study for steady and oscillatory current around a cylinder⁵⁴. The 2T
 26 mode is observed when the motion displacement reaches its maximum at the steady
 27 flow-dominated frequency. Away from this time periods, the double pair mode
 28 dominates (Figure 18 (a) and (d)). For the central smaller column, the vortex shedding
 29 is also dominated by waves but with a different pattern than the offset column. The KC
 30 number for the central column is 3.8, and the vortex is seen shed alternatively from one
 31 side of the column with an asymmetric pattern. Typically, this pattern occurs for a pure
 32 oscillatory with a cylinder when $KC > 4.0$ ¹⁶. However, in cases where a steady flow is
 33 present, this pattern is also observed at a smaller KC number.

34
 35

This is the author's peer reviewed, accepted manuscript. However, the online version of record will be different from this version once it has been copyedited and typeset.

PLEASE CITE THIS ARTICLE AS DOI: 10.1063/5.0158917

Accepted to Phys. Fluids 10.1063/5.0158917

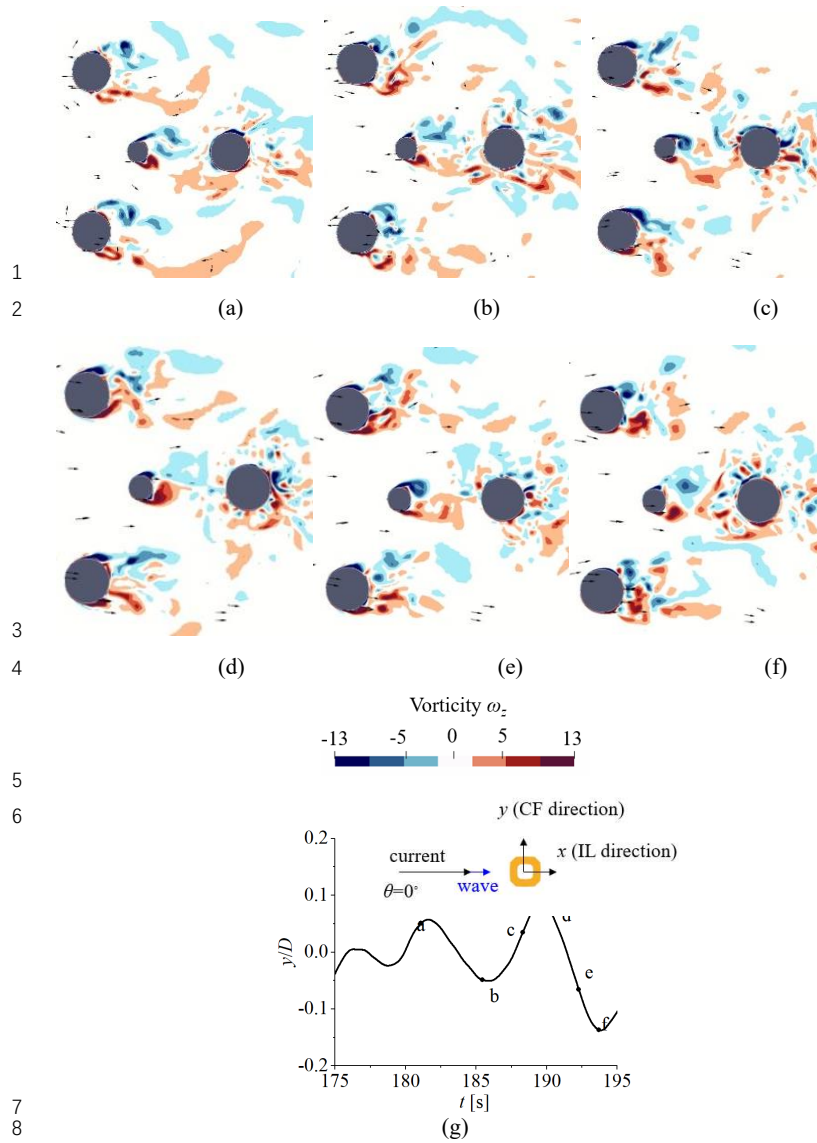


Figure 18. Contours of spanwise vorticity ω_z at the section with $z=-0.1\text{m}$ and $\theta=0^\circ$ in wave-current condition ($H=0.09\text{m}$ and $T=2.0\text{s}$) at different time instants at $V_r=8.1$ for (a) to (f), (g) is the corresponding time series, on top of which is the sketch of angle between wave and current

This is the author's peer reviewed, accepted manuscript. However, the online version of record will be different from this version once it has been copyedited and typeset.

PLEASE CITE THIS ARTICLE AS DOI: 10.1063/5.0158917

Accepted to Phys. Fluids 10.1063/5.0158917

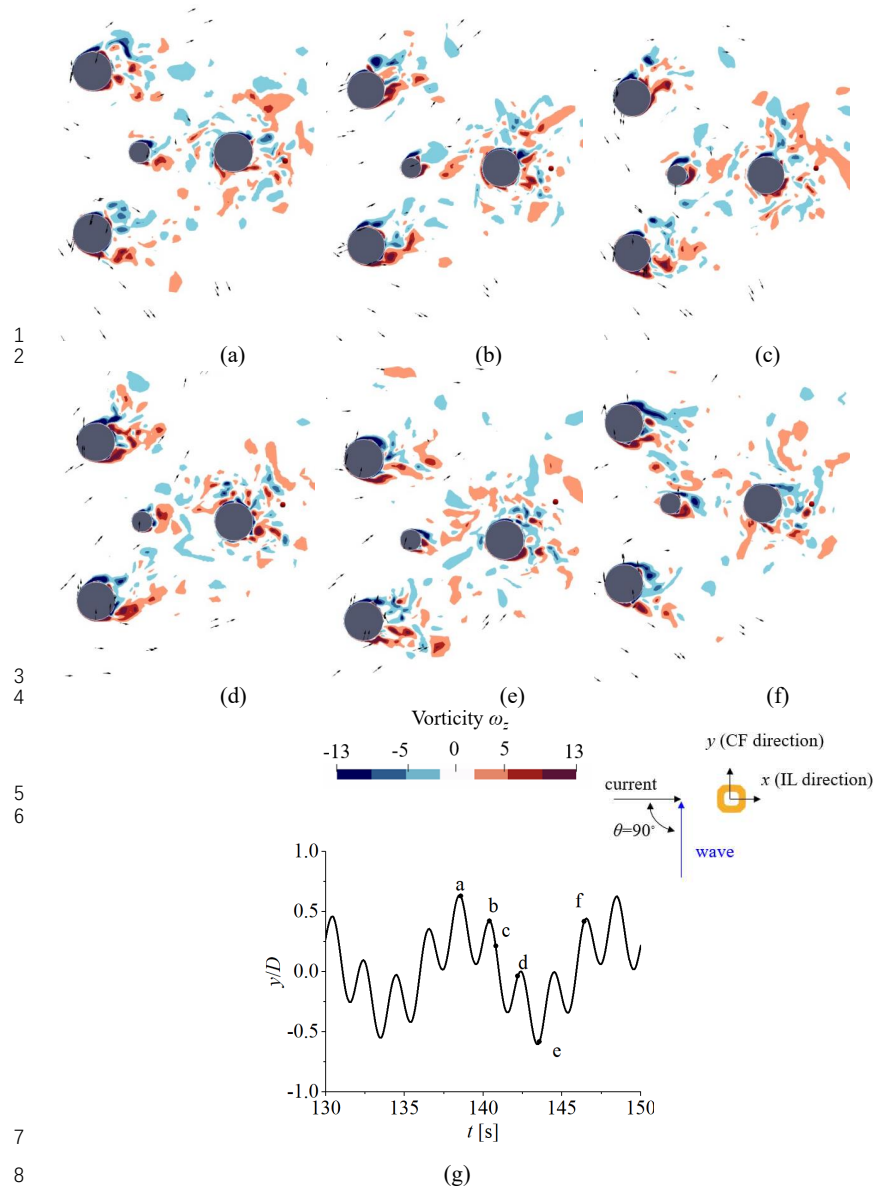


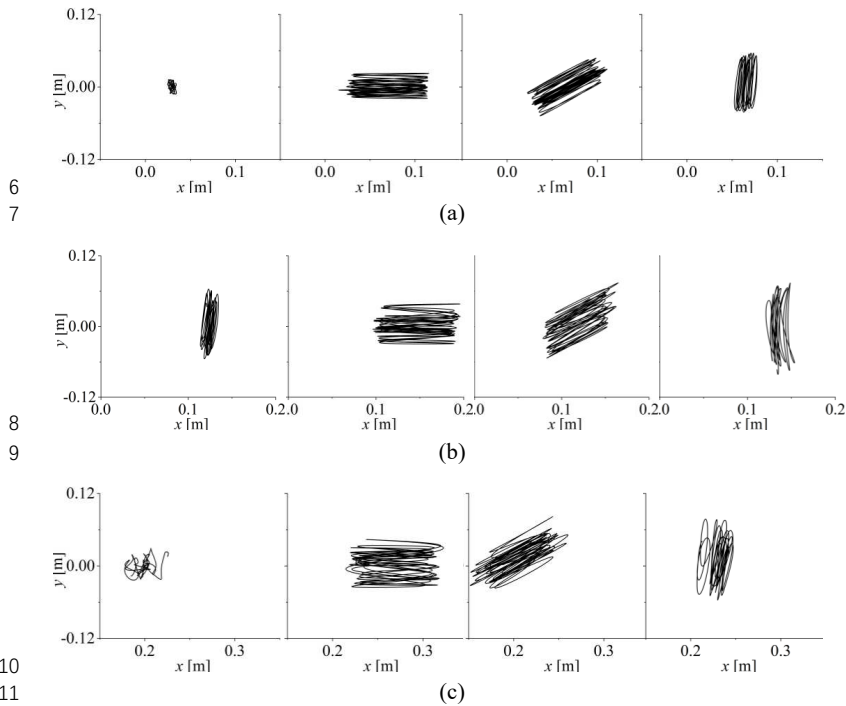
Figure 19. Contours of spanwise vorticity ω_z at the section with $z=-0.1\text{m}$ and $\theta=90^\circ$ in wave-current condition ($H=0.09\text{m}$ and $T=2.0\text{s}$) at different time instants from (a) to (f), at $V_i=8.1$, (g) is the corresponding time series, on top of which is the sketch of angle between wave and current

This is the author's peer reviewed, accepted manuscript. However, the online version of record will be different from this version once it has been copyedited and typeset.
 PLEASE CITE THIS ARTICLE AS DOI: 10.1063/5.0158917

Accepted to Phys. Fluids 10.1063/5.0158917

1 It should be noted that the symmetric vortex pair doesn't provide net force along CF
 2 direction, but it interferes with the vortex formed by the steady flow. Moreover, the
 3 flow in the $-x$ direction caused by the waves mitigates the generation of a complete
 4 vortex due to a steady current, leading to a possible reduction in crossflow motion.
 5

5



6

7

8

9

10

11

12

13

14

15

16

17

18

19

20

21

22

23

24

25

26

Figure 20. The trajectory of platform with current-only, wave-current condition ($H=0.09\text{m}$ and $T=2.0\text{s}$) with $\theta=0^\circ, 45^\circ$ and 90° at (a) $V_r=4.4$ (b) $V_r=8.1$ (c) $V_r=11.6$

Compared to the cases with $\theta=0^\circ$, the vortex field for $\theta=90^\circ$ in Figure 19 shows more asymmetric characteristics. Since the waves propagate along y -axis, the flow along x -axis is less affected. As a result, when a vortex forms, it is periodically stretched and carried by oscillatory flow in CF direction, causing it to split into smaller vortices. At $(y/D)_{\max}$ and $(y/D)_{\min}$ in Figure 19 (a) and (e), a large vortex is generated on one side of the offset column, but breaks down into small eddies. The vortex from the central small column presents a 2S mode with one clockwise and one counter-clockwise vortex detaching from the central column within one cycle. Moreover, the shed vortex not only moves downstream but also along CF direction, bringing it closer to the platform and increasing the chances of encountering between the clockwise and counter-clockwise vortices, thereby changing the motion frequency. This is clearly depicted from Figure 19 (b) to (c), where V_y is positive, while V_y is negative at Figure 19(f). It is clearly

1 indicated that when the wave and current are colinear, oscillatory flow mitigates the
 2 generation of a complete vortex due to current, thus the VIM is mitigated. The disturbed
 3 vortex field by the symmetric vortex from the oscillatory flow contributes to this trend.
 4

5 The platform motion trajectory with different θ and V_r is shown in Figure 20. For
 6 current-only cases, the platform experiences significant motion displacement within
 7 lock-in region at $V_r=8.1$. The predominant motion is along y -axis and the movement
 8 along x -axis is limited. This pattern of movement is similar to that in the study on a
 9 four-square column semi-submersible platform, where a typical eight-shaped trajectory
 10 is not found²⁵.
 11

12 **D. Response for $\theta=90^\circ$ with different wave parameters**

13
 14 Previous studies on colinear wave-current-structure interaction indicated that the CF
 15 response was not only affected by the reduced velocity, but also influenced by the wave
 16 parameters, i.e., the wave height and wave period (Gonçalves et al.^{35, 36}). In addition,
 17 our findings from Section C for various θ values reveal that the largest CF motion
 18 occurs at $\theta=90^\circ$. In this section, the investigation is focused on the study of wave-
 19 current-platform interaction at $\theta=90^\circ$ for a series of wave heights and wave periods
 20 (Table 6). The reduced velocity is fixed at $V_r=8.1$, where the strongest VIM occurs.
 21

22 The effect of wave parameters on the platform's response is shown in Figure 21. It is
 23 seen, IL motion is relatively small compared with the large platform dimensions. The
 24 overall CF motion is larger than that observed in the current-only cases and increases
 25 with wave period T . The motion response is also influenced by wave height H . As H
 26 increases, A_y/D approaches that of wave-only cases. A_y/D decreases monotonically with
 27 H for $T=1.5$ s. However, peaks are observed for $T=2.0$ s and $T=2.6$ s, the peak A_y/D is
 28 seen at $H=0.04$ m and 0.07 m, respectively. This concludes an important finding, e.g.
 29 waves with small wave height may also lead to large platform motion under wave-
 30 current condition.
 31

Wave height						Wave			
H [m]	0.116	0.09	0.07	0.04	0.02	period T [s]	1.5	2.0	2.63
Scaled 1:73						Scaled 1:73			
H [m]						T [s]			
Full-scale	8.4	6.5	5.1	3.0	1.5	Full-scale	12.8	17.6	22.6

32
 33 Table 6. Parameters for wave-current-platform interaction with OC4 platform on the
 34 effect of wave conditions with $\theta=90^\circ$
 35

This is the author's peer reviewed, accepted manuscript. However, the online version of record will be different from this version once it has been copyedited and typeset.

PLEASE CITE THIS ARTICLE AS DOI: 10.1063/5.0158917

Accepted to Phys. Fluids 10.1063/5.0158917

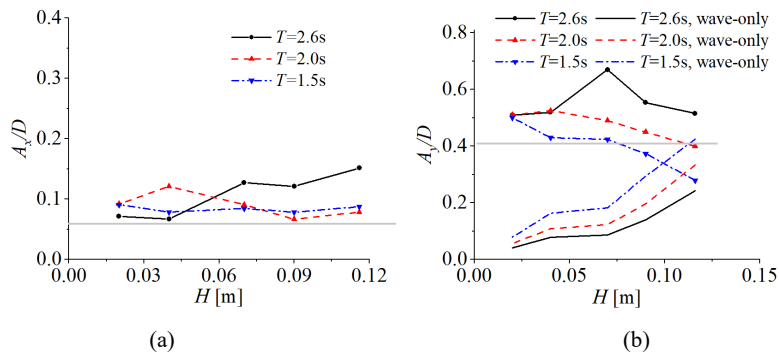


Figure 21. Response amplitude in wave-current condition with different wave heights and periods along (a) IL direction (b) CF direction, with $\theta=90^\circ$. The grey line indicates the motion amplitude with current-only.

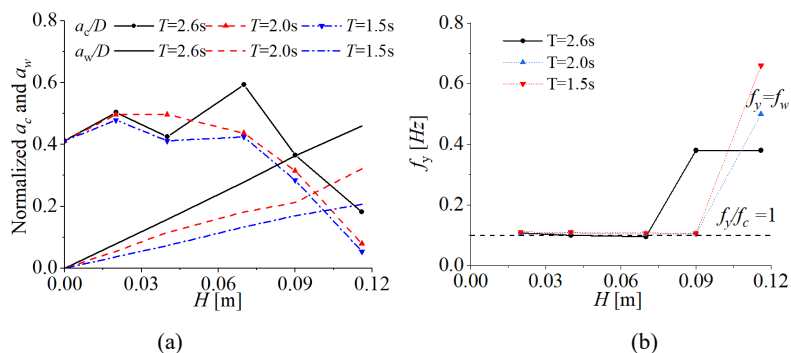
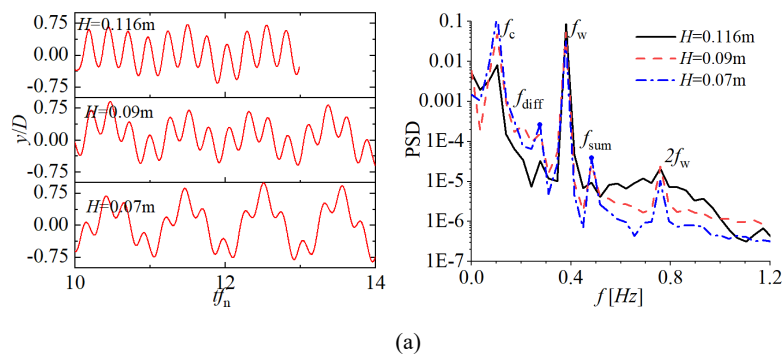


Figure 22. (a) Decomposed motion amplitude excited by current and waves (b) Dominant frequencies at $V_c=8.1$ with different wave parameters



(a)

This is the author's peer reviewed, accepted manuscript. However, the online version of record will be different from this version once it has been copyedited and typeset.

PLEASE CITE THIS ARTICLE AS DOI: 10.1063/5.0158917

Accepted to Phys. Fluids 10.1063/5.0158917

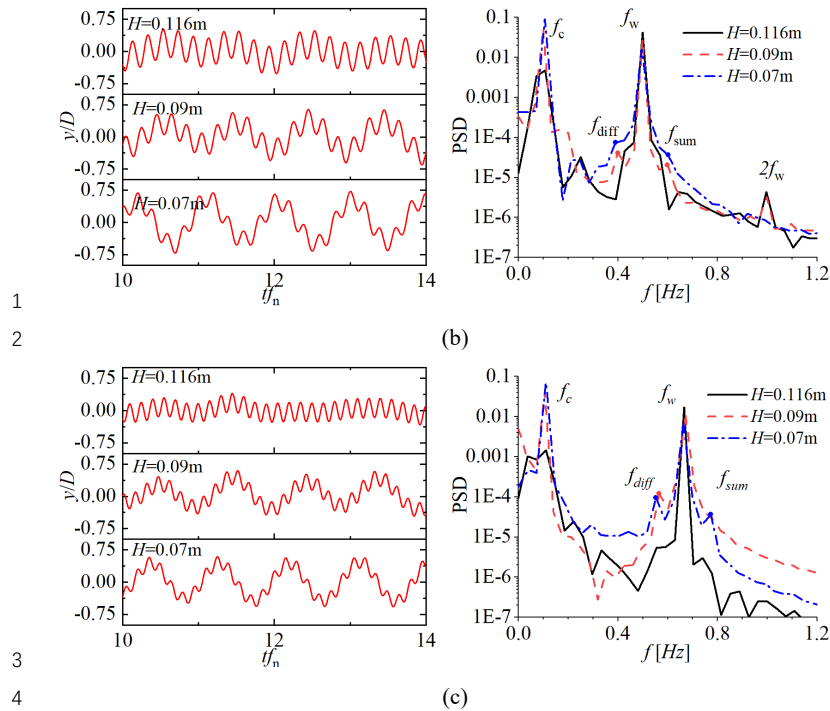


Figure 23. Time-series and FFT analysis of CF motion response in wave-current condition with $\theta=90^\circ$ at $V_r=8.1$ with (a) $T=2.6\text{s}$ (b) $T=2.0\text{s}$ (c) $T=1.5\text{s}$.

This can be further inferred by decomposing the motion amplitude shown in Figure 22(a). For cases with small $H < 0.06\text{m}$, the motion induced by current, indicated by a_c , varies between $0.4 < a_c/D < 0.5$, which is larger than that observed in current-only cases, indicating an enhanced VIM effect. However, for $H > 0.06\text{m}$, a_c decreases significantly with increasing H , indicating a mitigated VIM effect by waves. Meanwhile, a_w becomes dominant after $H > 0.11\text{m}$, and the motion is locked onto f_w rather than f_c , as shown in Figure 22(b). The shift in the predominant influence from currents to waves can also be observed from the time-histories of y/D and FFT plots in Figure 23. As H increases, the low-frequency motion induced by current becomes less prominent. The FFT analysis indicates the appearance of difference frequency and sum frequency components, especially for $\theta=90^\circ$. These frequencies are only excited when the contribution of current and wave to the system's energy is roughly equivalent. As H increases, the energy at f_c weakens, causing above two frequencies to become less significant.

This is the author's peer reviewed, accepted manuscript. However, the online version of record will be different from this version once it has been copyedited and typeset.

PLEASE CITE THIS ARTICLE AS DOI: 10.1063/5.0158917

Accepted to Phys. Fluids 10.1063/5.0158917

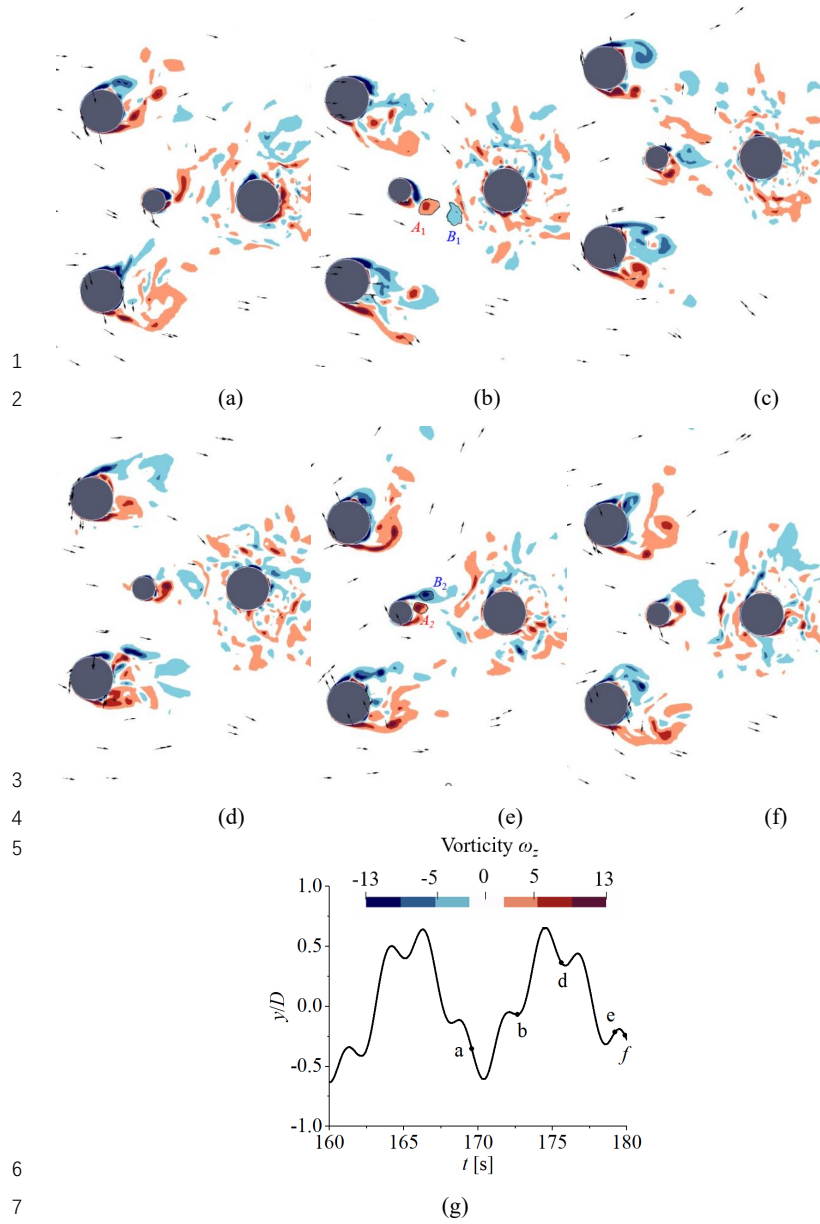


Figure 24. Contours of spanwise vorticity ω_z at the section with $z=-0.1\text{m}$ with $T=2.6\text{s}$ and $H=0.04\text{m}$ in wave-current condition with $\theta=90^\circ$ at $V_r=8.1$, at different time instants from (a) to (f), (g) is the corresponding time series

1
2
3

The differences in wave parameters are also reflected in the vorticity field shown in Figure 24 for $H=0.04\text{m}$. Compared with larger $H=0.09\text{m}$ in Figure 19, the vortex herein are less disturbed by waves, thus leading to a larger CF motion response. The vortex shedding appears a 2P mode, with 2 pairs of vortices shed in one cycle, such as the vortex A_1 and B_1 at instant b and A_2 and B_2 at instant e. As the wave period decreases, the vortex flow exhibits greater levels of turbulence and disorder, as seen from Figure 25(a) and (c). Additionally, the vortex motion is observed to occur in close proximity to the structure with smaller T .

11

According to Iwagaki, and Asano⁵⁵, velocity ratio can be an important parameter in the study of a combined wave-current environment. It is defined as⁵⁵:

14

$$\alpha' = \frac{\sigma_U}{\sigma_U + U} \quad (17)$$

15

where U and σ_U are the current velocity and the particle velocity amplitude in wave. With this definition, α' quantifies whether a flow is viscous or inertial dominant, and thus $\alpha'=1$ and 0 represent a wave-only or a current-only scenario, respectively. Previous study by Gonçalves et al.^{35, 36} for a semi-sub platform revealed that VIM is governed by both viscous and inertia forces. The threshold between the viscous and inertia zones can be quantified by:

21

$$KC = \frac{1+C_a}{C_d} \pi(\alpha')^2 \quad (18)$$

22

where C_a and C_d is the added mass and drag coefficient, which are 0.63 and 0.61 for OC4 Deepwind platform respectively⁵⁶.

24

Figure 26 plots velocity ratio (α') as a function of KC number with $\theta=90^\circ$. For the wave parameters examined, most cases are within a regime where VIM is obvious, thus associate with a large CF motion. For those falls into inertia force regime, the response is mainly wave-dominant.

29

It should be noted that, falling in the drag zone does not correspond to larger motion. For instance, the cases with a V_r beyond the lock-in region has a very small velocity ratio, and should be located in the drag zone. However, the absence of resonance leads to a smaller VIM amplitude. The interaction effect factor (IEF) is normally used to which is defined as

35

36

$$IEF = \frac{stddev(y_{wc})}{stddev(y_w) + stddev(y_c)} \quad (19)$$

37

where y_{wc} is the CF motion in wave-current combined environment, y_w and y_c is the CF motion in wave and current independently, $stddev$ means the standard deviation function. IEF can be viewed as the ratio between the amplitude of y_{wc} and y_w+y_c . For larger H and smaller T , the IEF becomes lower than 0.75 as shown in Table 7, suggesting that the interaction of waves and current mitigated the sum of their original

41

This is the author's peer reviewed, accepted manuscript. However, the online version of record will be different from this version once it has been copyedited and typeset.

PLEASE CITE THIS ARTICLE AS DOI: 10.1063/5.0158917

Accepted to Phys. Fluids 10.1063/5.0158917

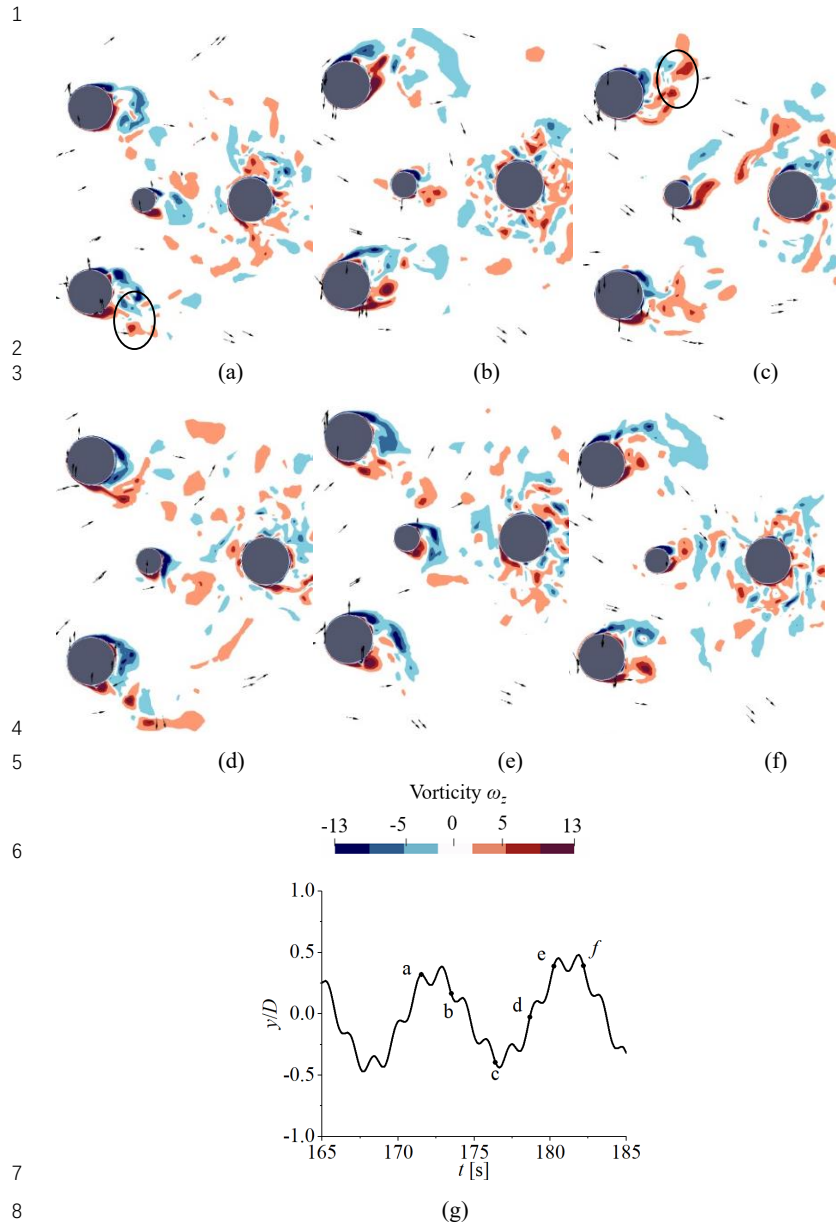


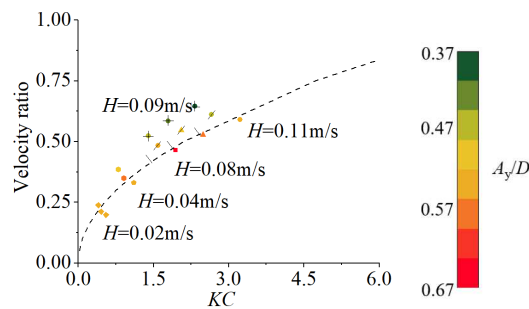
Figure 25. Contours of spanwise vorticity ω_z at the section with $z = -0.1\text{m}$ with $T = 1.5\text{s}$ and $H = 0.04\text{m}$ in wave-current condition with $\theta = 90^\circ$ at $V_r = 8.1$, at different time instants from (a) to (f), (g) is the corresponding time series

This is the author's peer reviewed, accepted manuscript. However, the online version of record will be different from this version once it has been copyedited and typeset.

PLEASE CITE THIS ARTICLE AS DOI: 10.1063/5.0158917

Accepted to Phys. Fluids 10.1063/5.0158917

1
2 motion. For small H and large T , the IEF is the largest and close to 1, which means the
3 motion can be considered as the sum of the motion in waves and current alone. For
4 some cases, the IEF exceeds 1 and reaches 1.35 when $H=0.07\text{m}$ and $T=2.6\text{s}$, indicating
5 that the motion is enhanced by the wave-current interaction. Special attention should
6 be paid to those cases when the extreme conditions for the platform are considered
7 during the design process.
8



9
10 Figure 26. α - KC plot with $\theta=90^\circ$ denoting predominant region of either drag or
11 inertia force in wave-current condition for OC4 platform. The point with colour
12 denotes CF motion response. The black line denotes the threshold between drag
13 range and inertia range.
14
15

$H[\text{m}]/T[\text{s}]$	1.5	2	2.6
0.02	1.02	1.09	1.13
0.04	0.75	1.01	1.06
0.07	0.72	0.92	1.35
0.09	0.53	0.74	1.01
0.116	0.34	0.54	0.79

16 Table 7. IEF with different wave parameters for $\theta=90^\circ$ and $V_c=8.1$
17

18 IV. Conclusion

19 This study explores the fluid-structure interaction of floating offshore wind turbines
20 under various scenarios, including wave-only, current-only, and wave-current
21 conditions in which the motion response is one of the main concerns. The CFD package
22 OpenFOAM with further developed models is used for the simulation. To reduce the
23 computational size for wave-current cases, a hybrid mesh and active wave absorbing
24 scheme are utilized. Comparison study shows that a semi-submersible platform has a
25 larger aspect ratio, exhibits a larger cross-flow (CF) motion and experiences the lock-
26 in phenomenon for the reduced velocities considered. Conversely, a barge platform,

This is the author's peer reviewed, accepted manuscript. However, the online version of record will be different from this version once it has been copyedited and typeset.

PLEASE CITE THIS ARTICLE AS DOI: 10.1063/5.0158917

Accepted to Phys. Fluids 10.1063/5.0158917

1 with a larger cross-surface area and low aspect ratio, shows a much smaller motion.
 2 Obvious vortex-induced motion (VIM) is not seen with selected V_r , indicating there is
 3 little chance for a floating barge platform undergoing a lock-in phenomenon.

4
 5 The angle between the directions of wave and current significantly affect the platform's
 6 CF motion, with a mitigated VIM and small CF motion being observed when the wave
 7 and current are colinear or having a small angle. Increasing the angle from 0° to 90°
 8 leads to a more significant VIM and larger CF motion, with the oscillation frequency
 9 being more synchronised with the system's natural frequency. The motion displacement
 10 reaches its maximum at angle of 90° , where the motion induced by wave and current
 11 are in the same direction and coupled nonlinearly. A combination of largest wave height
 12 and the most significant VIM does not result in the largest CF motion. The motion can
 13 be even larger for smaller wave height, in some cases. The study of Keulegan-Carpenter
 14 number (KC numbers) and velocity ratio shows that the motion is mitigated if the
 15 problem is inertia-force dominant and whereas motion will be enhanced if it is drag-
 16 force dominated.

17
 18 The interaction effect factor (IEF), which represents the motion ratio in wave-current
 19 condition compared to the sum motion in wave and current conditions separately, is
 20 evaluated. For large wave height and small wave period, the ratio is lower than 0.75,
 21 suggesting that the interaction of wave and current mitigates the sum of their individual
 22 motion. However, the most extreme motion does not necessarily take place with the
 23 largest wave height. With a smaller wave height, the ratio may be larger than 1.0.
 24 Remarkably, the interaction of wave and current could sometimes amplify the IEF to
 25 values as high as 1.35. At design stage of floating offshore wind turbines platforms,
 26 these coupling effects have generally not been accounted for though it sometimes
 27 critical as we illustrated. Therefore, our findings offer valuable insights for engineers
 28 considering the installation of wind turbines in regions where currents and waves
 29 coexist, potentially leading to more efficient and safer designs.

30
 31 Although with the above findings, one limitation of present study is the omission of
 32 wind loads and the resultant motion responses, critical elements in the interaction
 33 between FOWTs and current/waves. This is because the load generated by the upper
 34 turbine can alter the pitch and yaw motion, potentially influencing the vortex shedding
 35 around the structure. Although our current model does not include an aerodynamic
 36 simulation for wind turbines, future work is planned to expand the model's capabilities
 37 to address this aspect.

Acknowledgements

38
 39
 40 This work used the Cirrus UK National Tier-2 HPC Service at EPCC
 41 (<http://www.cirrus.ac.uk>) funded by the University of Edinburgh and EPSRC
 42 (EP/P020267/1) and ARCHIE-WeSt High-Performance Computer ([www.archie-](http://www.archie-west.ac.uk)
 43 [west.ac.uk](http://www.archie-west.ac.uk)) based at the University of Strathclyde. This research was supported by the

This is the author's peer reviewed, accepted manuscript. However, the online version of record will be different from this version once it has been copyedited and typeset.

PLEASE CITE THIS ARTICLE AS DOI: 10.1063/5.0158917

Accepted to Phys. Fluids 10.1063/5.0158917

1 National Natural Science Foundation of China (52271282, 51909189), Guangdong
2 Basic and Applied Basic Research Foundation (2022A1515010846) and Tsinghua
3 Shenzhen International Graduate School via the Scientific Research Start-Up Funds
4 (QD2021023C). Xiang Li thanks China Scholarship Council (CSC) and University of
5 Strathclyde (UoS) for financial support during his PhD study in the UK.

6

7

8

Reference

9

10 1. G. Stewart, and M. Muskulus, "A Review and Comparison of Floating Offshore Wind Turbine
11 Model Experiments," *Energy Procedia* **94**, 227 (2016).

12 2. C. M. Wang, T. Utsunomiya, S. C. Wee, and Y. S. Choo, "Research on floating wind turbines: a
13 literature survey," *The IES Journal Part A: Civil & Structural Engineering* **3**, 267 (2010).

14 3. M. A. Benitz, D. P. Schmidt, M. A. Lackner, G. M. Stewart, J. Jonkman, and A. Robertson,
15 *Comparison of hydrodynamic load predictions between reduced order engineering models and
16 computational fluid dynamics for the oc4-deepcwind semi-submersible* (American Society of
17 Mechanical Engineers, 2014).

18 4. H. Shin, *Model test of the OC3-Hywind floating offshore wind turbine* (OnePetro, 2011).

19 5. M. Borg, M. Walkusch Jensen, S. Urquhart, M. T. Andersen, J. B. Thomsen, and H. Stiesdal,
20 "Technical Definition of the TetraSpar Demonstrator Floating Wind Turbine Foundation," *Energies*
21 **13**, (2020).

22 6. Y. Liu, Q. Xiao, A. Incecik, C. Peyrard, and D. Wan, "Establishing a fully coupled CFD analysis tool
23 for floating offshore wind turbines," *Renewable Energy* **112**, 280 (2017).

24 7. Y. Zhou, Q. Xiao, Y. Liu, A. Incecik, C. Peyrard, S. Li, and G. Pan, "Numerical Modelling of Dynamic
25 Responses of a Floating Offshore Wind Turbine Subject to Focused Waves," *Energies* **12**, 3482
26 (2019).

27 8. Y. Zhou, Q. Xiao, C. Peyrard, and G. Pan, "Assessing focused wave applicability on a coupled
28 aero-hydro-mooring FOWT system using CFD approach," *Ocean Engineering* **240**, 109987 (2021).

29 9. J. Chen, Z. Liu, Y. Song, Y. Peng, and J. Li, "Experimental study on dynamic responses of a spar-
30 type floating offshore wind turbine," *Renewable Energy* **196**, 560 (2022).

31 10. F. Duan, Z. Hu, and J. Niedzwecki, "Model test investigation of a spar floating wind turbine,"
32 *Marine Structures* **49**, 76 (2016).

33 11. K. Kokubun, S. Ishida, T. Nimura, T. Chujo, S. Yoshida, and T. Utsunomiya, *Model experiment of
34 a SPAR type offshore wind turbine in storm condition* (American Society of Mechanical Engineers,
35 2012).

36 12. Q. Ding, C. Li, N. Yu, W. Hao, and J. Ji, "Numerical and experimental investigation into the
37 dynamic response of a floating wind turbine spar array platform," *Journal of Mechanical Science
38 and Technology* **32**, 1106 (2018).

39 13. A. J. Goupee, M. J. Fowler, R. W. Kimball, J. Helder, and E.-J. de Ridder, *Additional wind/wave
40 basin testing of the DeepCwind semi-submersible with a performance-matched wind turbine*
41 (American Society of Mechanical Engineers, 2014).

This is the author's peer reviewed, accepted manuscript. However, the online version of record will be different from this version once it has been copyedited and typeset.

PLEASE CITE THIS ARTICLE AS DOI: 10.1063/5.0158917

Accepted to Phys. Fluids 10.1063/5.0158917

- 1 14. A. J. Goupee, B. Koo, K. Lambrakos, and R. Kimball, *Model tests for three floating wind turbine*
- 2 *concepts* (OnePetro, 2012).
- 3 15. T. Sarpkaya, "A critical review of the intrinsic nature of vortex-induced vibrations," *Journal of*
- 4 *fluids and structures* **19**, 389 (2004).
- 5 16. B. M. Sumer, *Hydrodynamics around cylindrical structures* (World scientific, 2006).
- 6 17. Y. Bao, C. Huang, D. Zhou, J. Tu, and Z. Han, "Two-degree-of-freedom flow-induced vibrations
- 7 on isolated and tandem cylinders with varying natural frequency ratios," *Journal of Fluids and*
- 8 *Structures* **35**, 50 (2012).
- 9 18. R. T. Gonçalves, G. F. Rosetti, G. R. Franzini, J. R. Meneghini, and A. L. C. Fajarra, "Two-degree-
- 10 of-freedom vortex-induced vibration of circular cylinders with very low aspect ratio and small
- 11 mass ratio," *Journal of Fluids and Structures* **39**, 237 (2013).
- 12 19. M. Zhao, and L. Cheng, "Vortex-induced vibration of a circular cylinder of finite length," *Physics*
- 13 *of Fluids* **26**, (2014).
- 14 20. L. s. V. S. Sagrilo, M. Queija de Siqueira, T. A. n. Gonç, alves de Lacerda, G. B. Ellwanger, E.
- 15 Castro Prates de Lima, and E. N. Siqueira, *VIM and wave-frequency fatigue damage analysis for*
- 16 *SCRs connected to monocolumn platforms* (2009).
- 17 21. X. Liu, Z. Chen, Y. Si, P. Qian, H. Wu, L. Cui, and D. Zhang, "A review of tidal current energy
- 18 resource assessment in China," *Renewable and Sustainable Energy Reviews* **145**, (2021).
- 19 22. M. Cueva, A. L. Fajarra, K. Nishimoto, L. s. Quadrante, and A. P. Costa, *Vortex-induced motion:*
- 20 *model testing of a monocolumn floater* (2006).
- 21 23. R. T. Gonçalves, A. L. Fajarra, G. F. Rosetti, and K. Nishimoto, "Mitigation of vortex-induced
- 22 motion (VIM) on a monocolumn platform: forces and movements," *Journal of offshore mechanics*
- 23 *and arctic engineering* **132**, (2010).
- 24 24. R. T. Gonçalves, G. F. Rosetti, A. L. Fajarra, and K. Nishimoto, "An overview of relevant aspects
- 25 on VIM of spar and monocolumn platforms," *Journal of offshore mechanics and Arctic engineering*
- 26 **134**, (2012).
- 27 25. R. T. Gonçalves, G. F. Rosetti, A. L. C. Fajarra, and A. C. Oliveira, "Experimental study on vortex-
- 28 induced motions of a semi-submersible platform with four square columns, Part I: Effects of
- 29 current incidence angle and hull appendages," *Ocean Engineering* **54**, 150 (2012).
- 30 26. R. T. Gonçalves, M. E. F. Chame, L. S. P. Silva, A. Koop, S. Hirabayashi, and H. Suzuki,
- 31 "Experimental Flow-Induced Motions of a FOWT Semi-Submersible Type (OC4 Phase II Floater),"
- 32 *Journal of Offshore Mechanics and Arctic Engineering* **143**, (2021).
- 33 27. Z. Du, X. Li, W. Xu, H. Zhu, J. Feng, W. Shen, and R. Jin, "An experimental investigation on vortex-
- 34 induced motion (VIM) of a tension leg platform in irregular waves combined with a uniform flow,"
- 35 *Applied Ocean Research* **123**, 103185 (2022).
- 36 28. A. L. Fajarra, F. Cenci, L. S. Silva, S. Hirabayashi, H. Suzuki, and R. T. Goncalves, "Effect of initial
- 37 roll or pitch angles on the vortex-induced motions (VIM) of floating circular cylinders with a low
- 38 aspect ratio," *Ocean Engineering* **257**, 111574 (2022).
- 39 29. P. Jin, J. Liu, L. Xu, J. Wang, X. Ouyang, J.-H. Jiang, and J. Huang, "Tunable liquid–solid hybrid
- 40 thermal metamaterials with a topology transition," *Proceedings of the National Academy of*
- 41 *Sciences* **120**, e2217068120 (2023).
- 42 30. Y. Liu, F. Liu, Q. Xiao, and L. Zhou, "The effect of inclination on vortex-induced vibration of a
- 43 circular cylinder with a base column," *Ocean Engineering* **206**, (2020).
- 44 31. Y. Liu, D. Ge, X. Bai, and L. Li, "A CFD Study of Vortex-Induced Motions of a Semi-Submersible

This is the author's peer reviewed, accepted manuscript. However, the online version of record will be different from this version once it has been copyedited and typeset.

PLEASE CITE THIS ARTICLE AS DOI: 10.1063/5.0158917

Accepted to Phys. Fluids 10.1063/5.0158917

- 1 Floating Offshore Wind Turbine," *Energies* **16**, (2023).
- 2 32. V. Vinayan, A. Antony, J. Halkyard, S.-J. Kim, S. Holmes, and D. Spornjak, *Vortex-induced motion*
- 3 *of deep-draft semisubmersibles: A CFD-based parametric study* (American Society of Mechanical
- 4 Engineers, 2015).
- 5 33. H. Huang, H. Gu, and H.-C. Chen, "A new method to couple FEM mooring program with CFD
- 6 to simulate Six-DoF responses of a moored body," *Ocean Engineering* **250**, 110944 (2022).
- 7 34. H. Huang, and H.-C. Chen, "Investigation of mooring damping effects on vortex-induced
- 8 motion of a deep draft semi-submersible by coupled CFD-FEM analysis," *Ocean Engineering* **210**,
- 9 (2020).
- 10 35. R. T. Gonçalves, L. A. Pinto, and A. L. C. Fajarra, "Experimental study on vortex-induced motions
- 11 of a semi-submersible platform with four square columns, part III: Effects of the collinear irregular
- 12 and regular wave incidence and current," *Ocean Engineering* **217**, (2020).
- 13 36. R. T. Gonçalves, G. F. Rosetti, A. L. C. Fajarra, and A. C. Oliveira, "Experimental study on vortex-
- 14 induced motions of a semi-submersible platform with four square columns, Part II: Effects of
- 15 surface waves, external damping and draft condition," *Ocean Engineering* **62**, 10 (2013).
- 16 37. A. Maximiano, A. Koop, J. de Wilde, and R. T. Gonçalves, *Experimental study on the vortex-*
- 17 *induced motions (VIM) of a semi-submersible floater in waves* (American Society of Mechanical
- 18 Engineers, 2017).
- 19 38. X. Li, Q. Xiao, R. T. Gonçalves, and C. Peyrard, *A coupled wave-current-structure study for a*
- 20 *floating offshore wind turbine platform* (American Society of Mechanical Engineers, 2022).
- 21 39. I. Bayati, M. Belloli, L. Bernini, E. Fiore, H. Giberti, and A. Zasso, *On the functional design of the*
- 22 *DTU10 MW wind turbine scale model of LIFES50+ project* (IOP Publishing, 2016).
- 23 40. H. Jasak, A. Jemcov, and Z. Tukovic, *OpenFOAM: A C++ library for complex physics simulations*
- 24 (IUC Dubrovnik Croatia, 2007).
- 25 41. F. Nicoud, and F. Ducros, "Subgrid-scale stress modelling based on the square of the velocity
- 26 gradient tensor," *Flow, turbulence and Combustion* **62**, 183 (1999).
- 27 42. C. W. Hirt, and B. D. Nichols, "Volume of fluid (VOF) method for the dynamics of free
- 28 boundaries," *Journal of computational physics* **39**, 201 (1981).
- 29 43. P. Higuera, "Enhancing active wave absorption in RANS models," *Applied Ocean Research* **94**,
- 30 (2020).
- 31 44. X. Li, Q. Xiao, Y. Zhou, D. Ning, A. Incecik, R. Nicoll, A. McDonald, and D. Campbell, "Coupled
- 32 CFD-MBD numerical modeling of a mechanically coupled WEC array," *Ocean Engineering* **256**,
- 33 (2022).
- 34 45. Y. Liu, "A CFD study of fluid-structure interaction problems for floating offshore wind turbines,"
- 35 (2018).
- 36 46. K. M. A. Kosasih, H. Niizato, S. Okubo, S. Mitani, and H. Suzuki, *Wave tank experiment and*
- 37 *coupled simulation analysis of barge-type offshore wind turbine* (OnePetro, 2019).
- 38 47. L. Wang, A. Robertson, J. Jonkman, J. Kim, Z.-R. Shen, A. Koop, A. Borràs Nadal, W. Shi, X. Zeng,
- 39 E. Ransley, S. Brown, M. Hann, P. Chandramouli, A. Viré, L. Ramesh Reddy, X. Li, Q. Xiao, B. Méndez
- 40 López, G. Campaña Alonso, S. Oh, H. Sarlak, S. Netzband, H. Jang, and K. Yu, "OC6 Phase Ia: CFD
- 41 Simulations of the Free-Decay Motion of the DeepCwind Semisubmersible," *Energies* **15**, (2022).
- 42 48. X. Li, Q. Xiao, Y. Zhou, D. Ning, A. Incecik, R. Nicoll, A. McDonald, and D. Campbell, "Coupled
- 43 CFD-MBD numerical modeling of a mechanically coupled WEC array," *Ocean Engineering* **256**,
- 44 111541 (2022).

This is the author's peer reviewed, accepted manuscript. However, the online version of record will be different from this version once it has been copyedited and typeset.

PLEASE CITE THIS ARTICLE AS DOI: 10.1063/5.0158917

Accepted to *Phys. Fluids* 10.1063/5.0158917

- 1 49. Y. Liu, F. Liu, E. Wang, Q. Xiao, and L. Li, "The effect of base column on vortex-induced vibration
- 2 of a circular cylinder with low aspect ratio," *Ocean Engineering* **196**, 106822 (2020).
- 3 50. Y. Liu, D. Ge, X. Bai, and L. Li, "A CFD Study of Vortex-Induced Motions of a Semi-Submersible
- 4 Floating Offshore Wind Turbine," *Energies* **16**, 698 (2023).
- 5 51. M. Saito, S. Masanobu, T. Taniguchi, K. Otsubo, T. Asanuma, and K. Maeda, *Experimental*
- 6 *evaluation of VIM on MPSO in combined environmental conditions for waves and current*
- 7 (American Society of Mechanical Engineers, 2012).
- 8 52. T. Finnigan, M. Irani, and R. Van Dijk, *Truss Spar VIM in waves and currents* (2005).
- 9 53. T. Sarpkaya, "Force on a circular cylinder in viscous oscillatory flow at low Keulegan—Carpenter
- 10 numbers," *Journal of Fluid Mechanics* **165**, 61 (1986).
- 11 54. M. Zhao, K. Kaja, Y. Xiang, and G. Yan, "Vortex-induced vibration (VIV) of a circular cylinder in
- 12 combined steady and oscillatory flow," *Ocean Engineering* **73**, 83 (2013).
- 13 55. Y. Iwagaki, and T. Asano, *Hydrodynamic forces on a circular cylinder due to combined wave*
- 14 *and current loading* (1984).
- 15 56. A. Robertson, J. Jonkman, M. Masciola, H. Song, A. Goupee, A. Coulling, and C. Luan, Definition
- 16 of the semisubmersible floating system for phase II of OC4 Document No. Number, 2014.
- 17